Analysis of damped and fusion processes in the $^{197}Au+^{51}V$ reaction at $E_{lab}=447$ MeV

L. M. Schmieder, W. U. Schröder, and M. A. Butler*
Department of Chemistry and Nuclear Structure Research Laboratory, University of Rochester, Rochester, New York 14627
(Received 2 March 1987)

Angular, energy, and Z distributions of projectile-like and fission fragments were measured for the reaction $^{197}Au+^{51}V$ at $E_{lab}=447$ MeV. With increasing energy loss, the angular distribution evolves from a focused to an orbiting type, while the nearly Gaussian Z distributions broaden and drift to larger asymmetries. Extensive phenomenological analyses are presented for the angle-energy and charge-energy correlations. These data are compared in detail with results obtained from one-body transport model calculations. The effects of angular-momentum-dependent kinetic-energy fluctuations and of a reduced strength in the "wall friction" force are approximately taken into account. Good general agreement between data and model predictions is observed with friction forces of nominal strengths. The cross section for fusion-fission–like events, somewhat overestimated by the reaction model, is in reasonable agreement with the systematics provided by the "extra push" model parametrization.

I. INTRODUCTION

Studies of interactions between complex nuclei at energies of a few MeV nucleon above the barrier have yielded[1] a host of experimental information on the mechanism operating in damped or dissipative heavy-ion collisions. However, in spite of a considerable number of data sets available to date, several rather fundamental questions in regard to the damped reaction mechanism have remained open. For example, it has not yet been possible to distinguish experimentally between different sets of conservative, dissipative, and inertial forces proposed in the literature.[1] Although several dissipative features observed[1–16] in damped heavy-ion collisions can essentially be understood in terms of one-body, exchange-induced transport,[17,18] a possible coexistence of this mechanism with other stochastic[19–32] or collective[32–38] modes has not been ruled out by experiments and continues to present a challenging problem. At least partially, this deficiency in the current understanding of damped reaction mechanisms can be attributed to the lack of systematic comparisons of various reaction models to a large sample of experimental data. In addition, comparisons of different data have been made to the models, e.g., the one-body transport model, at different stages of implementation. For example, fluctuations other than those associated with mass and charge asymmetry are still receiving comparatively little attention in model calculations, although their influence may be noticeable.[39] In addition, the significance of suggestions[40,41] that the classical "wall formula,"[42] as used in the dynamical transport calculations, represents an unrealistic overestimate of the true (quantal) one-body dissipation rate, needs to be established.

The main purpose of this work is to report on experimental investigations of damped and fusion-fission–like $^{197}Au+^{51}V$ collisions at $E_{lab}=447$ MeV, and to discuss the implications of the measured fragment angular, energy, and charge distributions for the transport mechanisms occurring in such reactions. The present data on damped $^{197}Au+^{51}V$ collisions will be compared to previously observed[43,44] systematic trends in experimental charge-energy correlations and be analyzed in terms of classical phenomenological models. Extensive dynamical calculations[2,4] employing the one-body, exchange-induced transport theory proposed by Randrup[17,18] have been performed for the $^{197}Au+^{51}V$ reaction. The results of these calculations and the extent to which they are able to reproduce the data are discussed further below.

In particular, it will be shown that, at least in a simplified treatment, the effects of fluctuations in the total final kinetic energy associated with a given impact parameter do not appreciably change the degree of accuracy of data reproduction by the model. It is also seen that a sizable reduction in the effective strength of the "wall friction" force as suggested in the literature[40,41] would not provide an improved model description of experimental angle-energy and charge-energy correlations observed for the $^{197}Au+^{51}V$ reaction.

The reaction $^{197}Au+^{51}V$ is an interesting candidate for a study of nuclear reaction mechanisms, for several reasons. The system is rather asymmetric, providing the opportunity to study both the damped and the fusion-fission–like (FL) processes. The latter reaction type should occur with sizable probability, according to observations made[45,46] with other systems. At the bombarding energy of $E_{lab}=447$ MeV studied in this work, however, the damped reaction modes are expected[1] to dominate the cross section. As will be explained further below, the potential energy surface influencing the exchange of nucleons between the reaction partners possesses a shell-related minimum near the initial mass and charge asymmetries whose effect could be discernible in the charge distributions of projectile-like reaction fragments and their development with increasing energy dissipated in a collision. The extent to which mass and charge transfer between projectile-like and target-like

fragments in damped collisions at a few MeV per nucleon above the barrier is determined by such details of the energetics and the ground-state structure of the involved nuclei can be elucidated by comparing experimental results for the $^{197}Au + {}^{51}V$ reaction with those obtained for other asymmetric systems. It is of important practical consequence that the present reaction involves a heavy, neutron-rich target. For such systems, the decay of the primary projectile-like fragments is expected[1,14,47–49] to leave their atomic numbers essentially unaffected, while neutron evaporation is always a dominant mode of deexcitation[50] of the primary reaction fragments leading to sizable alterations in the fragment mass distributions that are difficult to assess without a knowledge of the multiplicities of the evaporated particles.

Section II outlines the experimental procedures employed in the present study. Results are described in Sec. III. Interpretations of the data in terms of phenomenological models as well as comparisons to dynamical reaction model calculations are given Sec. IV. Section V contains a summary.

II. EXPERIMENTAL PROCEDURES AND DATA ANALYSIS

The experiment was performed at the SuperHILAC accelerator of the Lawrence Berkeley Laboratory. A beam of $E_{lab}=447$ MeV ^{51}V projectiles was used to bombard a 300 $\mu g/cm^2$ thick, self-supporting ^{197}Au target. Damped projectile-like and fusion-fission fragments were detected in the laboratory angular range, $10° \leq \theta_{lab} \leq 55°$, using a solid-state $\Delta E - E$ telescope consisting of a 10.9 μm thick transmission detector and a 100 μm thick stop counter. The telescope was protected from δ electrons produced by the beam in the target, employing a 0.18 mg/cm^2 Ni-foil and rare-earth deflection magnets. Application of a high-voltage potential of ≥ 15 keV to the target, however, proved to be the most effective means to suppress such δ electrons. Two surface barrier monitor detectors were mounted symmetrically to the beam direction at a forward angle. They provided relative normalization of the data taken at different angles and were used to determine the dead time of counting electronics and computer, as has been discussed previously.[2] A standard electronic setup was employed, similar to the one described in Ref. 2.

Energy calibrations of the telescope were performed using a ThC α source and a precision pulse generator. They were checked against the energies measured for elastically scattered beam particles. Typical resolutions of 1.5% were obtained for the total energy of elastically scattered projectiles. The procedure suggested by Moulton *et al.*[51] was employed for correcting the apparent energies of reactions fragments, measured with the stop detector, for the pulse-height defect. No such correction was made for the thin transmission detector.

Conversion of the measured energy loss ΔE of a reaction product in the transmission detector to an atomic-number (Z) scale was accomplished, making use of experimental energy-loss curves for a similar detector, as reported by Hoover *et al.*[7] The mass-to-charge ratio of the projectile, $A_P/Z_P=2.22$, was used in the Z conversion procedure for all damped, projectile-like fragments. Z resolutions of approximately 1.4 units were obtained for such products.

Intensities for elastically scattered events were obtained from the experimental fragment energy spectra by either integrating the elastic peak directly or by fitting a standard line shape to the spectra measured for angles near and beyond the grazing angle. This procedure has been described previously.[1,2,4–8] Intensities for fusion-fission events were determined from the two-dimensional Z-E plots. These diagrams exhibited a broad intensity component centered in atomic number close to that corresponding to symmetric fragmentations ($\langle Z \rangle = 51$) and at an average laboratory energy of $\langle E \rangle \approx 196$ MeV. Fusion-fission–like events were distinguished from damped reaction products in a somewhat arbitrary fashion. A boundary between the two types of reaction products was defined in atomic numbers, as suggested by a valley appearing in the experimental Z distributions of events with relatively high energy losses in the region $Z=35$–41. Errors quoted for fusion-fission–like cross sections were estimated from the accuracy with which the above valley could be defined. In calculating these cross sections, account was also taken of the tails of the fusion-fission distribution corresponding to second kinematical solutions in calculating these cross sections, which appear at the lowest measured kinetic energies.

Damped reaction events were defined in accordance with the results of the fits to the elastic distribution and with the above definition of fusion-fission–like fragments. The experimental distributions were contaminated by slit-scattering events, especially at forward angles. Corresponding corrections were made to subtract these events from experimental spectra, but resulted in systematical uncertainties in the derived intensities for fragment atomic numbers in the vicinity of $Z=23$, which are difficult to estimate accurately. Consistency checks between the results for cross sections derived in various independent ways indicate, however, that the applied procedures did not lead to significant distortions of the true fragment distributions, as will be illustrated in Sec. III. Only the data obtained at the most forward angle of $\theta_{lab}=10°$ are contaminated to an extent that introduces large errors in the determination of the Z and energy distributions of damped fragments emitted at this angle.

Experimental Z-E fragment distributions resulting from the above procedure were then converted into the center-of-mass system, assuming a common mass-to-charge ratio of $A/Z=2.22$ for all fragments. The change in the average laboratory kinetic energy introduced by the evaporation of neutrons from the primary reaction fragments has been taken into account in the transformation, postulating, for the sake of calculating this correction, an equal partition of the dissipated kinetic energy among all nucleons of the system. Although a variation with energy loss of the primary A/Z value of fragments has been observed by Breuer *et al.*[47] in the case of ^{56}Fe-induced reactions, this variation is only of the order of 10% or less, too small to affect the average

results of the transformation of the present data to a significant extent. Transformed data for the cross section $\sigma(Z,\theta_{c.m.},E)$, obtained as a function of Z of the projectile-like fragment, its center-of-mass scattering angle $\theta_{c.m.}$, and the final total kinetic energy E in the center-of-mass system, were stored in a three-dimensional array. Various projections and subdivisions of these data are discussed in Sec. III.

III. EXPERIMENTAL RESULTS AND DISCUSSION

A. Elastic scattering

Although the process of elastic scattering of two complex nuclei is of considerable theoretical interest for a determination of nucleus-nucleus interaction potentials and the evaluation of the validity of various semiclassical pictures of the scattering process (see, e.g., Ref. 1), it is investigated for the present $^{197}Au + {}^{51}V$ reaction only in a cursory fashion, with the aim of deriving independent estimates of the total reaction cross section and of related quantities. The total reaction cross σ_R can be written as a sum over partial waves l, i.e.,

$$\sigma_R = \pi\lambda\!\!\!^{-2} \sum_l (2l+1)T_l \ . \tag{3.1}$$

Here, the quantity $\lambda\!\!\!^{-}$ is the deBroglie wave length for the relative motion, and T_l denotes the transmission coefficient describing absorption out of the elastic channel. The Fresnel model[52–54] and its extension[55] have been found[1] to give generally a good account of elastic-scattering angular distributions for heavy systems. In its simplest version, the Fresnel model is based on a sharp-cutoff model for the transmission coefficients T_l, where $T_l=1$ for l values smaller than the grazing angular momentum l_g, and $T_l=0$ for larger l values. For the generalized Fresnel model,[55] a smooth transition is assumed for the transmission coefficients, varying from $T_l=1$ to $T_l=0$ over a region in l space around $l=l_g$, characterized by a width parameter Δl. In this generalized model,

$$\sigma_R = \pi\lambda\!\!\!^{-2}(l_g+\tfrac{1}{2})^2\left[1+2\frac{\Delta l}{l_g+\frac{1}{2}}+\frac{\pi^2}{3}\left[\frac{\Delta l}{l_g+\frac{1}{2}}\right]^2\right] . \tag{3.2}$$

The angular distribution $d\sigma_{el}/d\Omega$ of the differential elastic-scattering cross section, given relative to the Rutherford cross section $d\sigma_{Ruth}/d\Omega$, can be expressed as

$$\frac{d\sigma_{el}(\theta)}{d\sigma_{Ruth}(\theta)} = \tfrac{1}{2}\{[\tfrac{1}{2}-S(W)]^2+[\tfrac{1}{2}-C(W)]^2\}F^2 + \begin{cases} 1+[C(W)+S(W)-1]F, & \theta<\theta_{1/4} \\ 0, & \theta>\theta_{1/4} \end{cases} \tag{3.3}$$

In Eq. (3.3), the quantities S and C denote the Fresnel sine and cosine integrals, respectively, to be taken for the argument

$$W=[(l_g+\tfrac{1}{2})/(\pi\sin\theta_{1/4})]^{1/2}\,|\,\theta-\theta_{1/4}\,| \ . \tag{3.4}$$

The function F appearing in Eq. (3.3),

$$F[\Delta l(\theta_{1/4}-\theta)]=\pi\Delta l(\theta_{1/4}-\theta)/\sinh[\pi\Delta l(\theta_{1/4}-\theta)] \ , \tag{3.5}$$

represents the Fourier transform of the elastic reflection function.

The angle $\theta_{1/4}$ appearing in the above equations is termed "quarter-point angle," since for $\theta=\theta_{1/4}$, $d\sigma_{el}/d\sigma_{Ruth}=\frac{1}{4}$. Assuming a Coulomb trajectory for a grazing-type collision leading to a scattering angle of $\theta=\theta_{1/4}$, this angle can be related to the characteristic strong-absorption or interaction radius

$$R_{SA}=\frac{\eta}{k}[+\csc(\tfrac{1}{2}\theta_{1/4})] \ , \tag{3.6}$$

which represents the distance of closest approach for such a trajectory. In Eq. (3.6) the quantities η and k stand for the Sommerfeld parameter and the inverse wave number, respectively.

Experimental results for the differential elastic scattering cross section, normalized to the calculated Rutherford cross section, are represented as circles in Fig. 1, plotted on logarithmic scale versus center-of-mass scattering angle $\theta_{c.m.}$. One observes an angular distribution typical of a heavy system. At forward angles, up to about $\theta_{c.m.}=40°$, there is little deviation of the experimental elastic cross section from the Rutherford formula, while the experimental cross section drops very rapidly at larger angles corresponding to smaller distances of closest approach. From interpolation of the experimental angular distribution, one obtains a quarter-point angle of $\theta_{1/4}=44.5°$ in the center-of-mass system, corresponding to a strong-absorption radius of $R_{SA}=13.4$ fm. These values, which agree well with the systematics[1] established for other reactions, are included in Table I, in

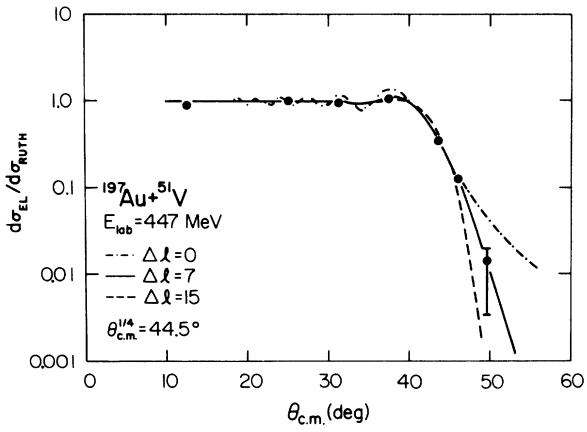

FIG. 1. Experimental ratio $d\sigma_{el}/d\sigma_{Ruth}$ of the elastic to Rutherford cross section is plotted vs center-of-mass scattering angle. The curves drawn through the data correspond to calculations using the generalized Fresnel model for widths in angular momentum space of $\Delta l=0$ (dotted-dashed), $\Delta l=7$ (solid), and $\Delta l=15$ (dashed).

TABLE I. Reaction parameters for the system $^{197}Au + ^{51}V$ at $E_{lab} = 447$ MeV.

E_{lab}	$=447\pm2.9$ MeV
$E_{c.m.}$	$=355\pm2.3$ MeV
$\theta_{1/4}$(lab)	$=35.7°\pm0.5°$
$\theta_{1/4}$(c.m.)	$=44.5°\pm0.5°$
μ(red. mass)	$=40.51$ u
K_∞(wave number)	$=26.67$ fm^{-1}
η(Coul. param.)	$=96.36$
R_{SA}(Fresnel)	$=13.4\pm0.2$ fm
l_g(Fresnel)	$=(236\pm3)\hbar$
σ_R(Fresnel)	$=2.7\pm0.2$ b
σ_R(expt.)	$=2.8\pm0.4$ b
$V_C(R_{SA})$	$=195$ MeV
$E_0 = E_{c.m.} - V_C(R_{SA})$	$=160$ MeV
$[E_{c.m.} - V_C(R_{SA})]/\mu$	$=3.95$ MeV/nucleon
σ(FL)	$=0.61\pm0.05$ b
l_{crit}	$=(115\pm8)\hbar$
l_{RLDM}	$=54\hbar$
$E_{c.m.}/V_B$	$=1.84$
$(Z^2/A)_{eff}$	$=35.35$
x_e	$=0.5996$

which global reaction parameters of interest for the system $^{197}Au + ^{51}V$ are collected. Most of the indicated errors have been estimated from uncertainties in the fits of the elastic cross section.

The experimental angular distribution of the elastic-scattering cross section is compared in Fig. 1 with the predictions of the Fresnel model for various width parameters Δl of the transmission function. As can be seen from this figure, the sharp-cutoff model yielding the dotted-dashed curve does not reproduce the data well at backward angles. At forward angles, it leads to oscillations in cross section not observed in the data. These oscillations dampen out when Δl is increased to 7 or 15. The corresponding theoretical angular distributions are represented in Fig. 1 by the solid and dashed curves, respectively. Obviously, a satisfactory description of the experimental distribution is obtained for $\Delta l = 7$. According to Eq. (3.2), this width corresponds to a total reaction cross section of $\sigma_R = 2.7$ b, in reasonable agreement with the direct integration of the measured reaction products, as discussed below. The range of width parameters Δl found to be compatible with the experimental elastic-scattering angular distribution for the $^{197}Au + ^{51}V$ reaction is consistent with values obtained[7] from an analysis of the $^{165}Ho + ^{56}Fe$ reaction. It contributes an error of $\sim\pm10\%$ to the uncertainty in estimating the total reaction section from the Fresnel-model analysis of elastic scattering of ^{51}V on ^{197}Au at $E_{lab} = 447$ MeV.

One should note that, in the above, an operational definition of the total reaction cross section was employed, as given by the adopted method of subdivision of experimental data into elastic and inelastic events. Obviously, due to the limited energy resolution of the detector, it was not possible to isolate ground-state-to-ground-state transitions and, hence, the events classified here as elastic include Coulomb and inelastic excitations associated with relatively small absolute Q values. To this extent, the figure σ_R obtained in this work for the $^{197}Au + ^{51}V$ reaction has to be considered an approximation to the total reaction cross section which, however, serves the present purpose well.[1]

B. Fusion-fission-like processes

Reactions between heavy nuclei resulting in fusion-fission-like (FL) distributions of symmetric final fragmentations and total kinetic energies constitute a topic of active current research.[45,56] The intermediate composite system produced in such a reaction with considerable spins is, according to the rotating-liquid-drop model[57] (RLDM), inherently unstable against fission. The limiting angular momentum of stability, beyond which the RLDM fission barrier for $^{197}Au + ^{51}V$ composite vanishes, is predicted to be $l_{RLDM} = 54\hbar$, significantly lower than the critical angular momentum, $l_{crit} = (111 \pm 8)\hbar$ derived in this work for the cross section for fusion-fission-like events. Such events were distinguished from damped $^{197}Au + ^{51}V$ collisions, as described in Sec. II. In Fig. 2, the angular distribution of the differential cross section $d\sigma/d\Omega$ is plotted versus center-of-mass reaction angle $\theta_{c.m.}$, as obtained in the present measurements. The relatively large errors shown at the data points reflect the systematical uncertainty associated with the distinction of FL reaction fragments. The dashed curve representing the functional form

$$d\sigma(\theta_{c.m.})/d\Omega_{c.m.} \propto (\sin\theta_{c.m.})^{-1} \tag{3.7}$$

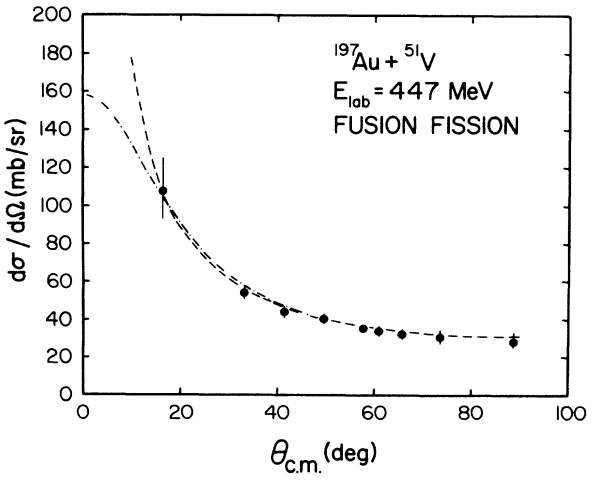

FIG. 2. Differential FL cross section $d\sigma/d\Omega_{c.m.}$ vs center-of-mass reaction angle $\theta_{c.m.}$. The dashed line represents a $(\sin\theta_{c.m.})^{-1}$-type curve; the dotted-dashed curve reproduces the angular distribution of FL fragments expected from the statistical scission model.

is observed to yield an excellent reproduction of the experimental data within the angular range explored in the measurements.

The theoretical expression of Eq. (3.7) applies to the classical situation of a fissioning system with a large spin I, aligned with a plane perpendicular to the beam direction.[58,59] It implies that transport mechanisms[17,60,61] operating during the collision are not effective enough to yield appreciable fluctuations in the alignment (tilting) of the fission axis of the intermediate system. The present measurements have not been carried out to angles forward enough to allow a distinction to be made between various models of fission fragment angular distributions. However, it is worth pointing out that the anisotropy of the angular distribution of fission fragments from the $^{197}Au + {}^{51}V$ reaction is considerable and strongly contradicts a picture in which a nearly spherical intermediate nucleus in statistical equilibrium decays with statistically oriented fission axes. This is in support of observations made[56,62–68] with other heavy systems.

In a more realistic "statistical scission model (SSM)" approach to FL reactions of heavy systems, Rossner *et al.*[56] assume that the angular distributions of FL fragments are determined by statistical fluctuations as they exist at the instance of scission of the intermediate double-nucleus system. The predictions of this model, employing the set of parameters suggested in the study of Rossner *et al.*,[56] is represented by the dotted-dashed curve in Fig. 2. This curve coincides with the $1/\sin\theta_{c.m.}$ distribution, within the measured range.

Extrapolating the measured angular distribution of FL fragments with the $1/\sin\theta_{c.m.}$ curve shown in Fig. 2 yields an integrated cross section of $\sigma(\mathrm{FL})=610\pm50$ mb, included in Table I. This uncertainty encompasses the cross section suggested by the SSM fit to the data. This integrated cross section agrees well with the predictions of parametrizations[1,45] of FL excitation functions based on Swiatecki's[69,70] "extra push" model that yield 660 mb for this quantity. For orientation, some of the parameters used in this "extra push" calculation are included in Table I, such as the effective Z^2/A ratio, the effective fissility x_e, and the bombarding energy expressed in units of the fusion barrier V_B. Dynamical calculations described in Sec. IV slightly overestimate the FL cross section for the present $^{197}Au + {}^{51}V$ reaction by approximately 100–150 mb.

C. Damped reactions

In the following, properties of damped $^{197}Au + {}^{51}V$ collisions are discussed, as manifested in angular, energy, and atomic-number distributions, derived from the measurement of the projectile-like reaction partners. Various correlations between experimental observables that have proven[1] characteristic of the microscopic reaction mechanisms will also be considered. Interpretations of the observed features in terms of quantitative models will be given in Sec. IV.

1. Integral fragment distributions

The laboratory angular distribution of the differential reaction cross section $d\sigma/d\Omega$ is plotted in Fig. 3 versus reaction angle θ_{lab}, as measured for damped projectile-like fragments with atomic numbers in the range $6 \le Z \le 40$, integrated over final total kinetic energy. As can be observed from this figure, a considerable fraction of the damped reaction cross section is focused into a narrow angular range, somewhat forward of the laboratory quarter-point angle of 35.7°. This focused component is superimposed on a broad, forward-rising cross section distribution. At the most forward angles, the angular dependence of the cross section is relatively uncertain, due to a large systematical error of the point at $\theta_{lab}=10°$, for which the data were significantly disturbed by slit-scattering contaminations. A curve is drawn through the data points in Fig. 3 to guide the eye. Its dashed part indicates the estimated continuation at forward angles.

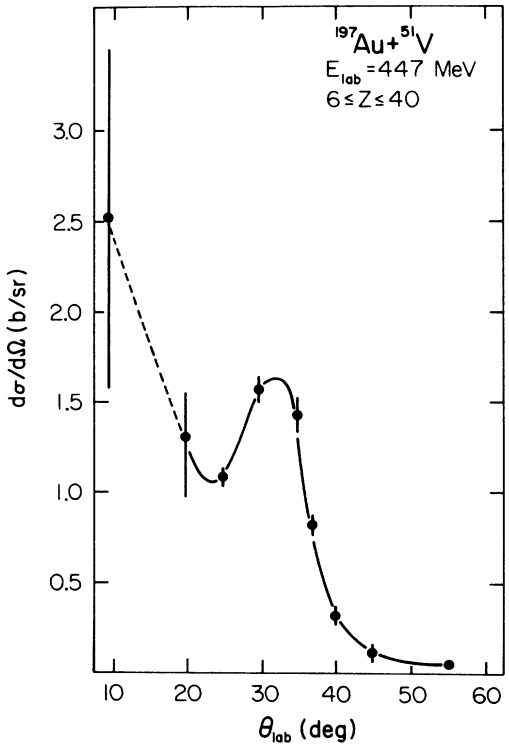

FIG. 3. Angular distribution $d\sigma/d\Omega$ of the projectile-like reaction products vs reaction angle θ_{lab}, excluding fusion-fission events. The solid line is drawn to guide the eye; the dashed line represents an estimate of the angular distribution at forward angles.

The angular distribution shown in Fig. 3 is typical[1] for medium-weight systems, where the Coulomb repulsion is not sufficiently strong to dominate the effective interaction potential for all values of initial angular momentum l. Hence, an l band exists for which the total entrance-channel potential has a minimum. Apart from a significant magnitude for the cross section for fusion-like events, such a property of the effective potential leads one to expect negative-angle scattering or orbiting to occur. The actual significance of orbiting-type processes depends[71] on the relative strengths of conservative and dissipative forces. Hence, the angular distribution ob-

served for a reaction offers a valuable opportunity to test friction-type reaction models. From early systematic studies,[1] one expects orbiting to be dominant for a reaction when the modified Sommerfeld parameter

$$\eta' = e^2 Z_P Z_T \{\mu/[2\hbar^2(E_{\text{c.m.}} - V_C)]\}^{1/2} \quad (3.8)$$

assumes values much smaller than $\eta' = 150$. Here, Z_P and Z_T are the atomic numbers of projectile and target, respectively, μ stands for the reduced mass of the system, while $E_{\text{c.m.}}$ and V_C denote the center-of-mass bombarding energy and the Coulomb energy at the strong-absorption radius, respectively. For the reaction $^{197}\text{Au} + {}^{51}\text{V}$ studied in this work at $E_{\text{lab}} = 447$ MeV, the modified Sommerfeld parameter turns out to be $\eta' = 144$ and , hence, a strong orbiting component is expected for this system.

Integrating the curve drawn through the data in Fig. 3, with a linear extrapolation to 0°, yields a value of $\sigma_D = 2.2 \pm 0.4$ b for the damped cross section. The considerable error in this value is largely due to the uncertainties of the experimental cross section at $\theta_{\text{lab}} = 10°$ and of its continuation to yet more forward angles. Combining damped and fusion-fission–like events yields a value of $\sigma_R = 2.8 \pm 0.4$ b for the total reaction cross section determined by such a direct integration of the corresponding angular distributions. This figure is in reasonable agreement with the value for the reaction cross section deduced from the analysis of elastic scattering discussed earlier. It lends confidence to the adequacy of the most important corrections made of the data, since these corrections have a drastically different effect for the evaluation of elastic and inelastic events.

The total charge distribution of projectile-like damped reaction fragments is plotted in Fig. 4 as $d\sigma/dZ$ versus fragment Z, integrated over the measured angular and final total kinetic energy (E) ranges indicated in the figure. A concentration of a large fraction of the cross section is noticeable in the Z distribution about Z values of 23, the projectile charge, and below. A broad tail of cross section extends towards the region of symmetric charge fragmentations. This latter feature is due to the onset of fusion-fission–like processes and other very strongly damped events.

The total kinetic energy loss (E_{loss}) distribution, determined from the measurement of projectile-like fragments, is represented by the histogram displayed in Fig. 5. The data are integrated over the charges of the light reaction partners in the range $6 \leq Z \leq 40$. The dashed histogram differs from the solid one in that an estimate has been made for the former distribution with respect to the contribution of data for angles of $\theta_{\text{lab}} = 10°$ and below, for which experimental results are ambiguous or lacking. In the energy loss distribution of Fig. 5, one observes a quasielastic peak at small values of E_{loss}, followed by a broad spectrum of damped events that extends to energy losses significantly higher than the kinetic energy, $E_0 = E_{\text{c.m.}} - V_C = 160$ MeV, available in the entrance channel. The cross section is seen to peak approximately at this energy E_0, which is indicated by the arrow in Fig. 5. Hence, a substantial fraction of the products emerge from the $^{197}\text{Au} + {}^{51}\text{V}$ reaction in a highly deformed state. Although large amounts of kinetic energy can be dissipated in the reaction, the cross section diminishes rapidly, as final total kinetic energies characteristic[72] of asymmetric fission are approached. This feature, which has also been observed[1] for other systems, could have its origin in the finite tensile strength of nuclear matter, precluding deformations of the intermediate system beyond a certain limit. Typical large deformations observed for the $^{197}\text{Au} + {}^{51}\text{V}$ reaction correspond to equivalent Coulomb repulsions of spherical fragments with surface separations of 5–10 fm.

2. *Correlations of experimental observables*

An overview of pertinent reaction features for the system $^{197}\text{Au} + {}^{51}\text{V}$ is provided by the Wilczyński diagram

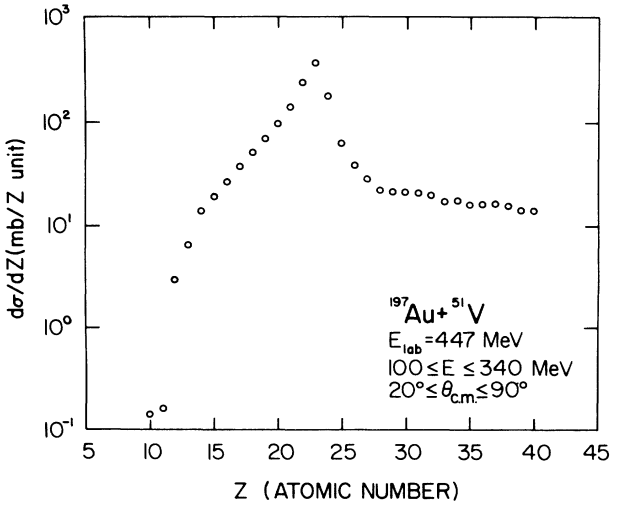

FIG. 4. Z distribution of projectile-like fragments, integrated over the indicated angular and total kinetic energy ranges.

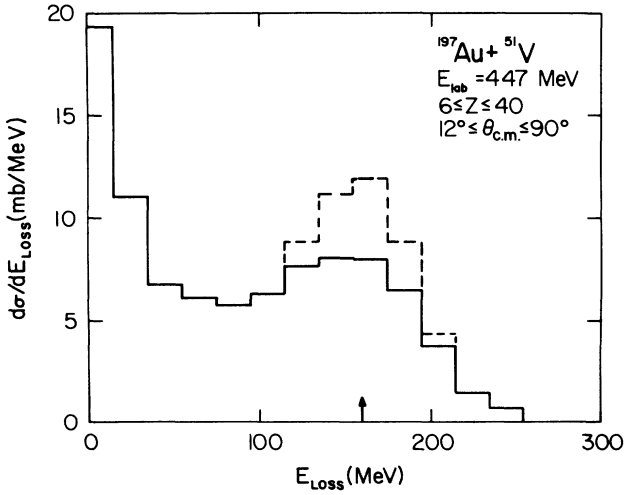

FIG. 5. Energy loss distributions for the damped events integrated over fragment angle and charge. The dashed part of the figure represents the estimated contribution of data for angles $\theta_{\text{lab}} \leq 10°$. The arrow indicates the available kinetic energy in the entrance channel, $E_0 = E_{\text{c.m.}} - V_C(R_{\text{SA}})$.

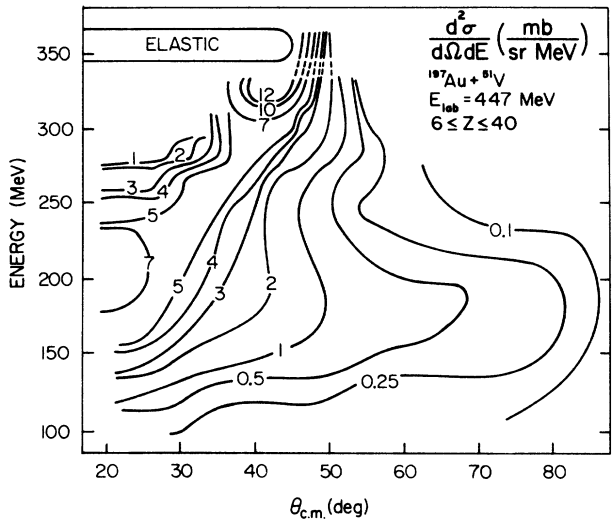

FIG. 6. Contour diagram of the double-differential cross section $d^2\sigma/d\Omega_{c.m.}dE$ plotted vs center-of-mass scattering angle and total kinetic energy (Wilczyński diagram).

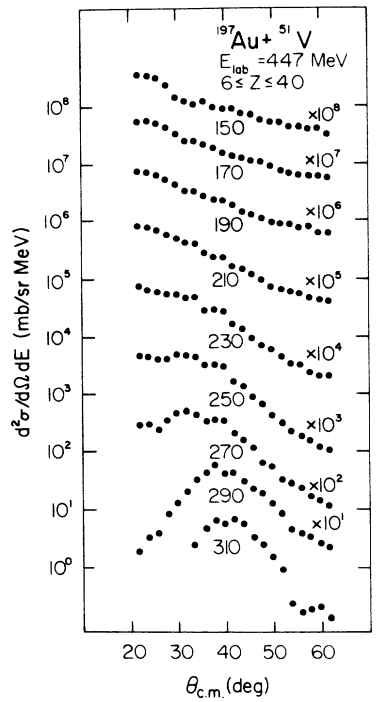

FIG. 7. Angular distributions $d^2\sigma/d\Omega_{c.m.}dE$ as a function of center-of-mass reaction angle. The energy bins are 20 MeV wide. The data are integrated over $6 \leq Z \leq 40$.

displayed in Fig. 6. Here, the double-differential cross section $d^2\sigma/d\Omega\, dE$ is represented in terms of a contour diagram, plotted versus center-of-mass reaction angle $\theta_{c.m.}$ and the final total kinetic energy E. A ridge of cross section is observed to develop from the elastic and quasielastic region near the quarter-point angle, moving to forward angles, with final kinetic energies approaching the entrance-channel Coulomb barrier V_C. A local cross section maximum is observed at small angles at this energy. This maximum could be due to the superposition of the forward-going cross section ridge and its continuation on the other side of the beam, which, in the experimental plot of Fig. 6, is seen to extend towards large backward angles. The above interpolation in terms of the orbiting picture appears reasonable[1] in the light of results of polarization experiments performed for a number of projectile-target systems. It is also supported by the dynamical calculations presented in Sec. IV.

It should be emphasized that the contour diagram displayed in Fig. 6, as well as others to be discussed below, have been smoothed somewhat, as there is considerable latitude in the way average contour lines of constant cross section can be drawn. Such diagrams serve here only illustrative purposes to enhance the average trends observed in the data.

Angular distributions used to construct the Wilczyński diagram of Fig. 6 are exhibited in Fig. 7. Here, the double-differential damped cross sections $d^2\sigma/d\Omega\, dE$ are plotted versus center-of-mass angle, for various bins of final total kinetic energy. The central energies (in MeV) and scaling factors are indicated at the distributions in Fig. 7. From this figure, one observes that fragment angular distributions are peaked a few degrees forward of the quarter-point angle of $\theta_{1/4}(\text{c.m.})=44.5°$. As the energy loss is increased, the distributions broaden significantly. They approach an approximately exponential distribution which is most clearly defined for energies smaller than $E=210$ MeV. In this respect, even the most strongly damped processes are clearly distinguished from fusion-fission–like reaction associated with $1/\sin\theta_{c.m.}$-type angular distributions.

The phenomenon observed for the angular distributions in Fig. 7 for large energy losses is typical for an orbiting situation, as discussed by Bondorf *et al.*[71] These authors consider the angular distribution associated with l waves close to the critical angular momentum for fusion, l_{crit}. Here, the deflection function $\theta(l)$ exhibits a logarithmic singularity, corresponding to an exponential angular distribution of the form

$$d\sigma/d\theta \propto 2\pi\lambda\!\!\!^{-2} l_{crit}^2 \exp[(\theta-\theta_C)/y] \ . \tag{3.9}$$

In Eq. (3.9) the quantity y is a measure of the relative strength of the frictional force assumed in the model with respect to the conservative force, and θ_C corresponds to the sum of Coulomb deflection angles in entrance and exit channels. The predicted exponential decrease of the angular distribution becomes more gradual with increasing strength of the friction force, reflecting an increased lifetime of the intermediate system.

Although in Fig. 7 angular distributions are plotted as $d\sigma(\theta_{c.m.})/d\Omega\, dE$, rather than $d\sigma(\theta_{c.m.})/d\theta_{c.m.}$, their dependence is approximately consistent with the general shape predicted by Eq. (3.9), for intermediate and high energy losses. It is interesting to note that the slope of the experimental angular distributions does not depend on the energy loss for final energies smaller than $E=210$ MeV. This behavior is quite different from that observed[73] for ^{12}C and ^{16}O induced reactions at somewhat

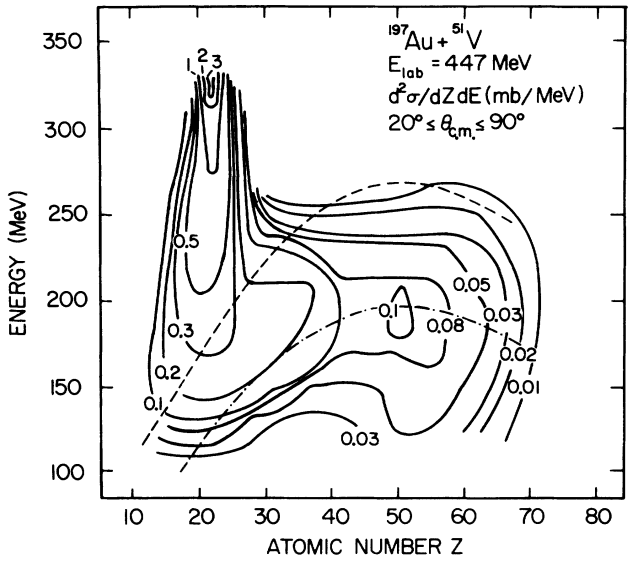

FIG. 8. Contour diagram of the double-differential cross section $d^2\sigma/dZ\,dE$ plotted vs total kinetic energy E and fragment charge Z, integrated over angle. The dashed curve represents the Coulomb barrier V_C for touching spheres and for different fragmentations. The dotted-dashed line indicates the Coulomb energy for elliptically deformed final fragments.

higher energies, for which definite correlations between energy loss and slope parameters y were reported. However, such differences are not unexpected, because of the system and energy dependence of conservative forces acting in damped reactions.

Of particular interest for a study of transport phenomena in damped reactions are the correlations observed between fragment Z distributions and the amount of kinetic energy dissipated in a collision. Figure 8 shows the double-differential cross section $d^2\sigma dZ\,dE$ plotted versus final total kinetic energy E and detected fragment atomic number Z. The data displayed in this contour diagram, also known as "diffusion plot," have been integrated over all angles and include fusion-fission–like events. Starting from the atomic number of the projectile and quasielastic energies, the cross section is observed to develop a ridge which is almost parallel to the energy axis. As the total kinetic energy is increased, the ridge broadens and moves slightly to smaller Z values. One also observes a broad cross section bump centered at fragment charges corresponding to symmetric splits of the composite system. It is located at an energy of about 190 MeV, in agreement with the Viola systematics[72] of the total kinetic energy release in low-energy fission. For comparison, the Coulomb energy for spherical reaction partners touching at their strong-absorption radius is indicated by the dashed curve in Fig. 8. Also included in this figure is the Coulomb energy (dotted-dashed curve) calculated for elliptically deformed final fragments according to Brack *et al.*[74] As is apparent from Fig. 8, there is, in general, no clear correlation of iso-cross-section contour lines with the Coulomb energies for spherical or deformed fragments, with the exception of the region of fusion-fission–like events. For the most strongly damped events, this observation implies that deformations of the constituents of the intermediate system develop as charge is transferred. In particular, the strong Z dependence of the calculated Coulomb energy appears to present no barrier that could inhibit proton pickup by the projectile-like reaction partner. Hence, the Coulomb interaction energy does not seem to play a significant role for the charge exchange mechanism operating in damped ^{197}Au + ^{51}V collisions. This observation in quite in contrast to conclusions drawn by Rudolf *et al.*[75] in their study of the somewhat heavier system ^{166}Er + ^{86}Kr, but agrees with the more general trends[1] of many systems.

The importance of the degree of kinetic energy damping for the evolution of the fragment Z distributions is illustrated in Fig. 9(a). Here, individual distributions $d^2\sigma/dZ\,dE$ are plotted versus fragment charge, for various 10-MeV wide bins of final total kinetic energy. The distributions have been multiplied by the scaling factors given on the right-hand side of each data set to effect a separation along the logarithmic ordinate. It is apparent from Fig 9 that the energy-differential Z distributions are rather well described by Gaussian shapes illustrated by the solid curves representing fits to the data points. For intermediate and high energy losses, asymmetric tails develop towards larger Z values, but their relative cross sections are by more than an order of magnitude smaller than those corresponding to the main part of each Z distribution. This minimal deviation from the basically Gaussian shape of the Z distributions shown in Fig. 9 for the ^{197}Au + ^{51}V reaction is remarkable in comparison to those observed for other systems such as ^{165}Ho + ^{56}Fe.[7] This is possibly due to the larger initial asymmetry of the ^{197}Au + ^{51}V system making the region around the projectile charge numbers less susceptible to contaminations from the wings of the Z distribution of fusion-fission–like events. Nevertheless, distributions corresponding to final energies at or below the entrance-channel Coulomb barrier are significantly distorted by fusion-fission–like contaminations. They are, therefore, omitted from further consideration.

As can be inferred from the Gaussian fits to the Z distributions displayed in Fig. 9, there is only a weak dependence of the centroids of these Gaussians on the amount of dissipated energy. For large energy losses, the centroids have drifted only by 2 Z units away from the initial Z value of the projectile towards asymmetry. A considerable broadening of the Gaussian Z distributions occurs, however, as the total kinetic energy loss increases.

Differential fragment charge distributions displayed in Fig. 9(b) represent projections of cuts through the diffusion plot of Fig. 8 corresponding to constant energies above or below the Coulomb energy $V_C(Z_L,Z_H)$ of spherical fragments touching at their strong-absorption radius (dashed curve in Fig. 8). Here, Z_L and Z_H are the atomic numbers of the final fragments. The associated modified energy loss parameter $E^*_{\rm loss}$ is related to the total kinetic energy loss $E_{\rm loss}$ according to

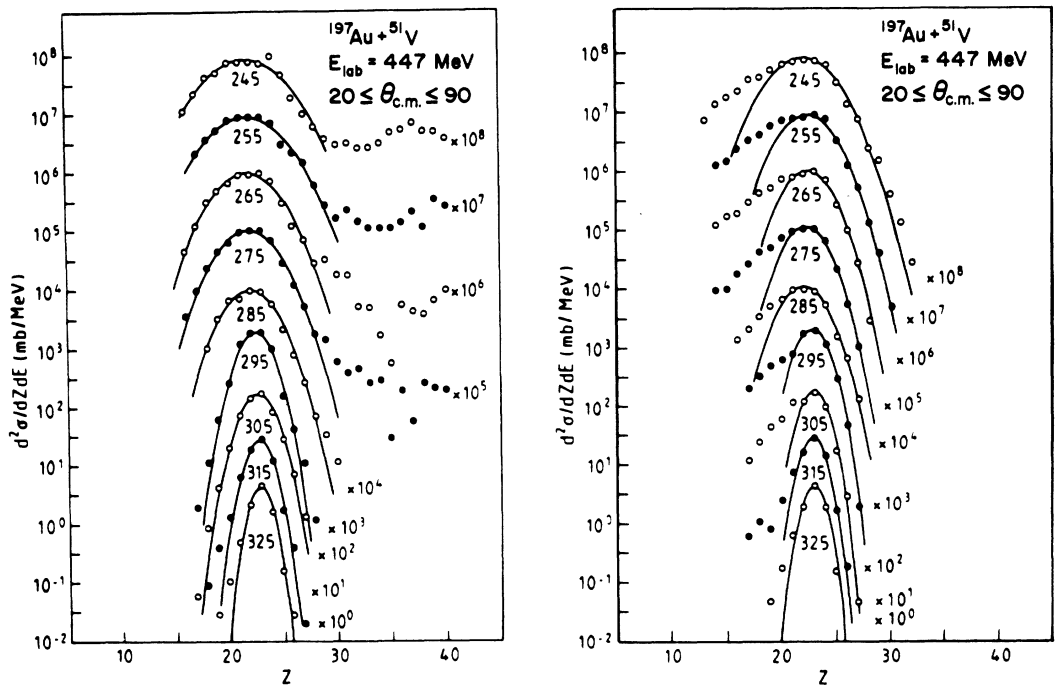

FIG. 9. Fragment Z distributions plotted for different values of the total kinetic energy, as indicated in the figure. The energy bins are 10 MeV wide. The distributions have been multiplied by the factors indicated on the right-hand side of each curve. The solid lines represent Gaussian fits to the data. The set of curves in the right-hand part of the diagram corresponds to cuts through the diffusion plot parallel to the Coulomb energy of spherical fragments (dashed curve in Fig. 8).

$$E^*_{\text{loss}}(Z_L,Z_H)=[E_{\text{c.m.}}-V_C(Z_P,Z_T)] -[E-V_C(Z_L,Z_H)]\ . \tag{3.10}$$

The energy values given at each distribution correspond to the final kinetic energy E for the initial charge fragmentation. The appearance of the fragment charge distributions shown in Fig. 9(b) is quite different from that of the spectra exhibited in Fig. 9(a). While the latter are well described in terms of Gaussians, this is true only for the high-Z wings of the distributions in Fig. 9(b), developing significant asymmetries already for small energy losses. Similar analyses applying Coulomb corrections in the cases of fragment Z distributions for the $^{166}\text{Er}+{}^{86}\text{Kr}$ reaction[75] and for $^{165}\text{Ho}+{}^{56}\text{Fe}$ collisions[7] have yielded distributions that are better described by Gaussians than those resulting from binning with respect to total kinetic energies or energy losses. The present results for the $^{197}\text{Au}+{}^{51}\text{V}$ reaction indicate that an argument in favor of analyses in which data are sorted with respect to modified energy parameters cannot be justified consistently by the symmetry of the resulting fragment charge distributions. Nevertheless, the distributions in Fig. 9(b) resulting from this type of analysis will be briefly considered further in the following. Hence, Gaussian fits have also been made for these distributions, as indicated by the solid curves in this figure. Satisfactory representation of the experimental data is only achieved for the high-Z wings of the experimental Z spectra.

Numerical results for the first and second moments, $\langle Z\rangle$ and σ_Z^2, respectively, obtained from Gaussian fits to the experimental distributions of Fig. 9, are depicted in Figs. 10 and 11. Here, the fit values and their uncertainties are plotted versus total kinetic energy loss, E_{loss}, and modified energy loss parameter, E^*_{loss}, respectively. The variances σ_Z^2 have been corrected for the experimental Z resolution. Solid and dashed curves drawn through the data represent the results of dynamical calculations discussed in Sec. IV.

Although the moments of the charge distributions for

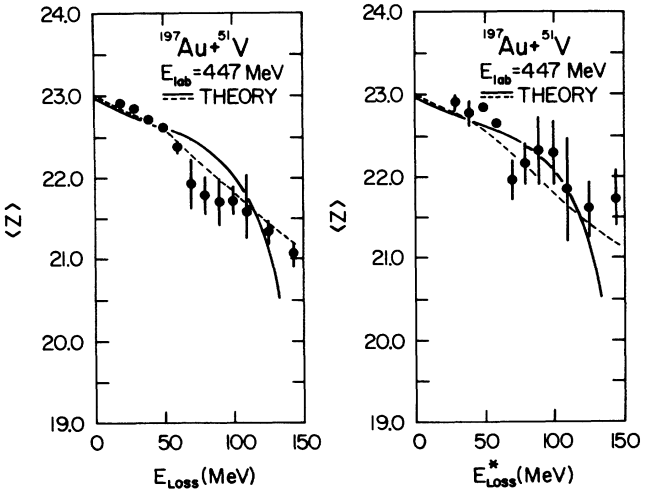

FIG. 10. Centroids of the fragment charge distributions $\langle Z\rangle$ plotted vs E_{loss} and modified energy loss parameter E^*_{loss}, respectively. The solid and dashed lines represent the results of a dynamical model calculation.

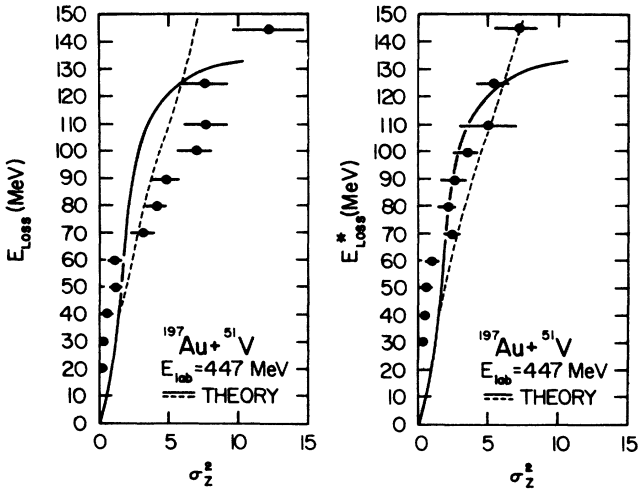

FIG. 11. Comparison of experimental correlations between the total kinetic energy loss E_{loss} or modified parameter E^*_{loss}, and the variances σ^2_Z of the fragment Z distributions with predictions of dynamical model calculations (solid and dashed lines).

the projectile-like component shown in Figs. 10 and 11 are derived from data integrated over all angles, these values are representative of the fragment Z distribution measured for small bins of center-of-mass reaction angle $\theta_{c.m.}$. Figure 12 illustrates the angular independence of the full width at half maximum (FWHM) of the Z distributions for various selected bins of final kinetic energy. It is seen from this figure that the widths of the Z distributions for individual angles $\theta_{c.m.}$ are well described by the results obtained from fits to angle-integrated distributions. These latter values are represented by horizontal lines in Fig. 12. This feature, which has also been found[1] for a few other damped reactions that were analyzed in detail, seems to be universal and demonstrates the dominant role of the energy loss parameter as an indicator of the stage of evolution of a damped collision. This role is understood in terms of an energy transfer mechanism mediated by friction-type forces, which results in increasing energy losses as the interaction time proceeds. The broadening of angular and charge distributions with increasing energy loss is, in this picture, simply reflective of increased lifetimes of the intermediate system available for rotation and mass exchange.

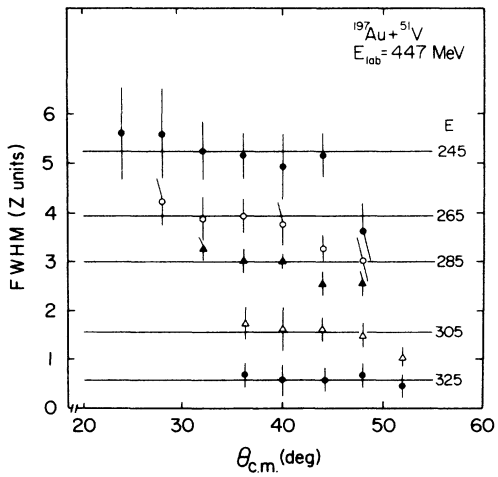

FIG. 12. Widths (FWHM) of the fragment Z distribution versus reaction angle, for five 10 MeV wide energy bins. The horizontal lines represent fits to the angle-integrated Z distributions (cf. Fig. 9).

IV. INTERPRETATION OF EXPERIMENTAL RESULTS

A. l-wave decomposition and interaction times

To understand the dependence of damped reaction observables on impact parameter and their evolution with progressing time of interaction is a fundamental goal of phenomenological analyses. Such analyses are made with the help of simplified classical reaction models[1] that employ correlations between experimental observables and rely on a minimum of independent assumptions. They are useful also in emphasizing hidden trends in the data.

A concept that is often employed in classical or semiclassical reaction models, viewing the interaction of complex nuclei in terms of potential scattering under the influence of classical friction forces, refers to the average classical deflection function $\theta(l)$. Here, θ is the average center-of-mass reaction angle and l denotes the entrance-channel angular momentum. The reaction angle is, of course, an experimental observable, while a correlation has to be assumed between the unobserved angular momentum and a measurable quantity. It is physically appealing, as well as consistent[1] with current microscopic reaction models, to assume[2] an average monotonic relation between initial l value and the amount of kinetic energy dissipated in a collision. Large initial l values, in the vicinity of the grazing angular momentum l_g, are in this picture associated with negligible energy losses. The energy loss increases with decreasing angular momentum leading to more deeply interpenetrating collisions and longer lifetimes of the intermediate system. For the time being, fluctuations in this correlation will be neglected. They will be discussed in Sec. IV C. Assuming further for simplicity that the measured damped reaction cross section is related to the initial l value according to a sharp cutoff model, one can deduce from the cross section $\Delta\sigma_{ij}$ measured for a given total kinetic energy window $[E_i,E_j]$, a corresponding l window $[l_i,l_j]$, where

$$l_i=[(l_j+1)^2-\Delta\sigma_{ij}/(\pi\lambda\!\!\!^{-2})]^{1/2}-1\ . \tag{4.1}$$

Starting with $l_1=l_g(E_{c.m.})$, i.e., neglecting small energy losses associated with grazing collisions, one can successively generate the functions $l(E)$ or $E_{loss}(l)$.

Results of the above l-wave decomposition of the damped reaction cross section, measured in the reaction $^{197}Au+^{51}V$, are displayed in the bottom part of Fig. 13, where the average total kinetic energy loss E_{loss} is plotted versus the centroid of the associated l window. The errors drawn at the data points reflect the uncertainty in

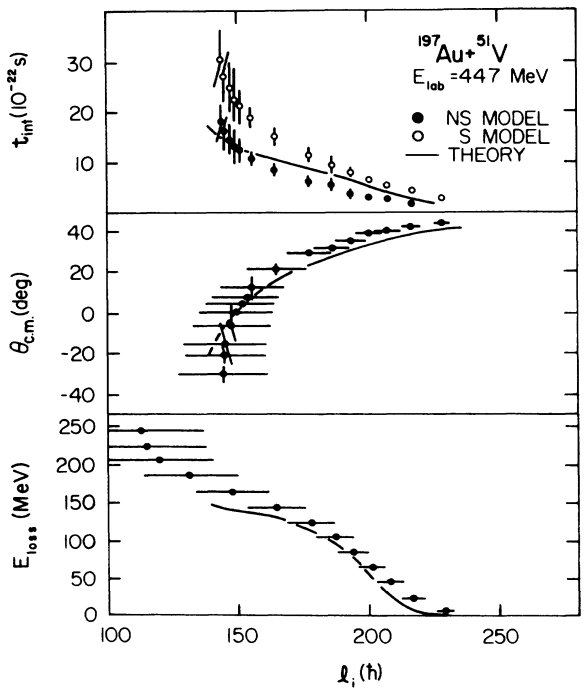

FIG. 13. Empirical correlations of total kinetic energy loss, deflection angle, and interaction time with initial angular momentum are compared to a trajectory calculation (solid lines).

determining the grazing angular momentum and the cross sections in the quasielastic and strongly damped regions. The character of the deduced relation $E_{\text{loss}}(l)$ is as expected from the shape of the cross section $d\sigma/dE_{\text{loss}}$ plotted in Fig. 5. Since

$$\frac{dE_{\text{loss}}}{dl} = -\pi\lambda^2(2l+1)(d\sigma/dE_{\text{loss}})^{-1} , \tag{4.2}$$

the shape of $d\sigma/dE_{\text{loss}}$ is reflected in the integral function $E_{\text{loss}}(l)$ only by a small undulation about a straight-line correlation. A linear E_{loss} dependence of $d\sigma/dE_{\text{loss}}$ would result[1] in a constant slope dE_{loss}/dl of the correlation displayed in Fig. 13.

Having deduced an approximate transformation between energy loss and angular momentum, it is possible to derive an average deflection angle from the experimental Wilczyński diagram shown in Fig. 6. This is possible at least for the forward-going cross section ridge, where a definite correlation exists between average reaction angle and energy loss. The procedure leads to less well-defined results for the backward-going, orbiting-type ridge which is almost parallel to the angle axis. Therefore, a smooth interpolation was made in the region $-42° \leq \theta_{\text{c.m.}} \leq +22°$ between the forward-going and the orbiting ridge, which was taken to represent negative scattering angles. The resulting experimental average deflection function is displayed in the middle part of Fig. 13. It is obvious from this figure that for l values close to the grazing angular momentum the deflection function is rather flat. This corresponds to the Coulomb rainbow, where the differential cross section has a maximum. As the l value decreases, the reaction angle becomes smaller, approaching $\theta_{\text{c.m.}}=0°$ for l values close to $l=150$. For even smaller angular momenta, negative-angle scattering sets in. The actual orbiting singularity should occur in the region of $l \approx 100-120$, according to the present estimates of the critical l value for fusion.

Angular-momentum-dependent interaction times $t_{\text{int}}(l)$ were determined, employing a simple classical reaction model proposed earlier.[2] In this model, the reaction partners are assumed to approach each other on Coulomb trajectories up to the Rutherford distance of closest approach or the strong-absorption distance R_{SA}, whichever is largest. At this point, the kinetic energy of radial motion is assumed to have been dissipated, and the intermediate system rotates under the influence of the nuclear interaction. The rotation angle $\Delta\theta$ is determined from the difference between the experimental deflection angle for each l value and the sum of entrance- and exit-channel Coulomb deflection angles, which can be calculated analytically. The dinuclear system is assumed to break apart and continue on a Coulomb trajectory at a separation distance consistent with the measured final kinetic energy. This energy is a sum of Coulomb repulsion and centrifugal energies. The interaction time is then estimated as

$$t_{\text{int}}(l) = \Delta\theta(l) J/(\hbar l_f) . \tag{4.3}$$

Here, $J=\mu R_{\text{SA}}^2$ is taken as an effective average moment of inertia for the orbital motion of the dinuclear system. Separation distances r both larger and smaller than $r=R_{\text{SA}}$ are expected to occur on each actual trajectory. The quantity l_f in Eq. (4.3) denotes the final orbital angular momentum. As the two limiting cases, the sliding and sticking situations are considered in the evaluation of the interaction time. In the sliding case, angular-momentum dissipation is neglected, such that $l_f=l$. In the other extreme of a sticking collision, leading to rigid rotation of the dinuclear system, the orbital angular momentum is reduced to

$$l_f = lJ/J_{\text{RB}} . \tag{4.4}$$

Here, the rigid-body moment of inertia

$$J_{\text{RB}} = \mu R_{\text{SA}}^2 + \tfrac{2}{5}(M_P R_P^2 + M_T R_T^2) \tag{4.5}$$

is calculated from the masses, M_P and M_T, and the matter radii, R_P and R_T, of the projectile and target, respectively.

The resulting l-dependent interaction times are plotted in the top portion of Fig. 13 versus initial angular momentum. They are seen to vary from a few times 10^{-22} s, associated with near-grazing collisions, to several times 10^{-21} s, for the most strongly damped collisions. Sticking and sliding models lead to differences of the order of a factor of 2 in these estimates. The interaction times deduced for the $^{197}Au + ^{51}V$ reaction are of the same order as those derived[2-9] for other reactions. They are rather short, even as predicted by the sticking-model analysis. For comparison, rotational periods of $t(\Delta\theta=2\pi)=(3-5)\times10^{-21}$ s can be estimated

for the range of l values explored in the $^{197}Au + {}^{51}V$ reaction.

B. Systematical features of charge-energy correlations

In order to put the present results on fragment Z distributions into perspective with observations made for other reactions, it appears useful to compare the measured energy loss dependence of the variance, σ_Z^2, in the Z distribution of projectile-like fragments from the reaction $^{197}Au + {}^{51}V$ with the results of global fits performed in the systematical study of Wollersheim *et al.*[43,44] In this study, it was found that the dependence of σ_Z^2 on bombarding energy $E_{c.m.}$ and an effective temperature T of the system can be cast into the approximate form[44]

$$\sigma_Z^2(T)=\exp\left[3.465\frac{(A_P+A_T)^{3/2}}{R_{SA}(A_P A_T)^{1/2}}\frac{T^2}{(E_{c.m.}-V_C)^{1/2}}\right]. \tag{4.6}$$

Here, A_P and A_T are the mass numbers of projectile and target, respectively, and V_C is the entrance-channel Coulomb energy, evaluated at the strong-absorption radius R_{SA}. In Eq. (4.6) the temperature is calculated from the Fermi gas formula, i.e., $T=[8E^*/(A_P+A_T)]^{1/2}$.

Theoretical relations predicted by Eq. (4.6) are exhibited in Fig. 14 for two slightly different definitions (solid and dashed curves) of the temperature parameter in terms of initial and final total kinetic energies. They are compared to experimental data for the present $^{197}Au + {}^{51}V$ system (solid dots). One observes from this figure that the parametrization according to Eq. (4.6) is able to reproduce the average trend in the experimental correlation $\sigma_Z^2(E_{loss})$, but fails to account for the quantitative details of the data.

In the systematical studies[43,44] of the dependence of experimental fragment Z distributions on the final energy E, it is also suggested that the double-differential cross section $d^2\sigma/dE\,dZ$ separates into a Gaussian charge distribution and an energy dependent normalization factor $N(E)$. For this latter factor, a systematical parametrization is offered[44] in the form

$$N(E)=b(E-V_C^{def})$$
$$=0.0324\left[R_{SA}^2/E_{c.m.}-0.19\ \frac{mb}{MeV}\right](E-V_C^{def}). \tag{4.7}$$

Here, the various quantities are the bombarding energy $E_{c.m.}$, the strong-absorption radius R_{SA}, and the Coulomb energy V_C^{def} of deformed fragments at the scission point.

The dotted-dashed and dotted lines in Fig. 15 correspond to the general parametrization of Eq. (4.7), where values for the Coulomb energy V_C^{def} have been estimated from the fission systematics[72] and from the limiting energy where in the experimental Wilczyński diagram of Fig. 6 the scattering angle becomes uncorrelated with final energy, respectively. The associated energies are $V_C^{def}=200$ and 185 MeV, respectively. The numerical value of the slope parameter is predicted by the above systematics to be $b=1.03\times10^{-2}$, whereas a fit to the data points represented by the solid curve in Fig. 15 yields the significantly smaller value of $b_{expt}=5.9\times10^{-3}$.

The differences observed in Figs. 14 and 15 between the experimental energy loss dependencies of differential cross section and charge variances and those predicted by systematics[43] may be characteristic of the extent to which the systematics can be considered universal. They also reflect the sensitivity of the resulting parametrizations on details of the analysis. These discrepancies, then, do not imply that the gross reaction features of damped $^{197}Au + {}^{51}V$ collisions are substantially different from those associated with other reactions. The most general trends of the experimental energy-differential cross sections and charge variances can be explained[1] simply in terms of a damped reaction mechanism occur-

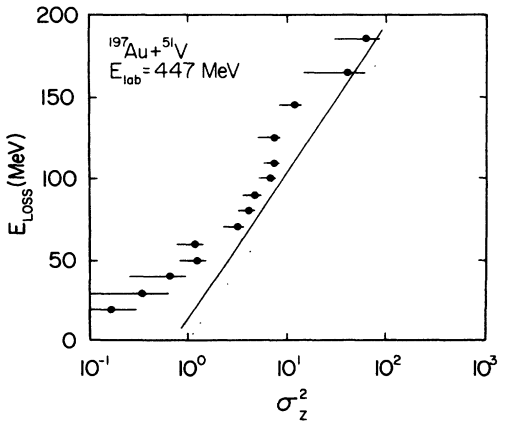

FIG. 14. Experimentally deduced variances σ_Z^2 vs energy loss E_{loss}. The lines result from calculating σ_Z^2 with Eq. (4.7), assuming $E^*=aT^2=E_{loss}$ (solid curve) and $E^*=aT^2=E_0'-E$ (dotted line).

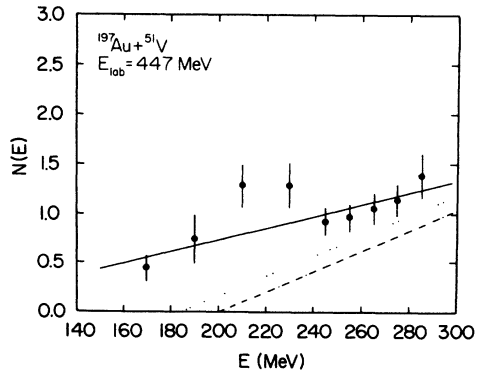

FIG. 15. Gaussian normalization function $N(E)$ vs total kinetic energy, as calculated from experimental values of charge variance $\sigma_Z^2(E)$ and energy loss spectrum $d\sigma/dE$. The solid line represents a least-squares fit to the data. The dotted line indicates the predictions derived from the systematics for several other reactions, assuming $V_C^{def}=185$ MeV. The dotted-dashed line has the same slope as the dotted curve, but corresponds to an energy of $V_C^{def}=200$ MeV.

ring with a continuous interval of final energies which decrease from the initial energy $E_{\text{c.m.}}$ with decreasing angular momentum l. However, it is not this gross, qualitative behavior of the reaction features that allows one to draw conclusions about the microscopic origin of the damped reaction mechanism, but the quantitative characteristics of the functional dependence of experimental correlations that contain this information. Hence, a significant role in the evolution of mass exchange processes in damped reactions can generally not be attributed[43,44] to the temperature T of the interacting system or its level density, based merely on a qualitative reproduction of experimental charge-energy correlations by systematics such as represented by Eq. (4.6).

C. Dynamical model calculations

A major theoretical effort in heavy-ion reaction studies has been devoted to the development of transport theories for the description of mass exchange and energy dissipation.[1] The various models differ considerably with respect to the choice of collective reaction variables and the microscopic origin assumed of the transport processes occurring in damped reactions. In the following, the data obtained in this work for the $^{197}\text{Au} + {}^{51}\text{V}$ reaction at $E_{\text{lab}} = 447$ MeV will be compared to the predictions of the transport theory proposed by Randrup.[17,18]

In the above dynamical reaction model, transport of mass, charge, and energy are effected entirely by the stochastic exchange of independent nucleons between the constituents of the dinuclear complex formed in a damped collision. The dinuclear system is described in terms of dumbbell-like shapes determined by the set of parameters illustrated in Fig. 16. These include the separation distance r, the neck radius ρ, the radii R_P and R_T of the fragments, their orientation angles θ_P and θ_T, the angle θ describing the overall orientation of the dinuclear system, mass (A), and atomic (Z) numbers of one of the fragments, and the nuclear temperatures of both fragments.

Average values $\{\bar{q}_i, \dot{\bar{q}}_i\}$ of the macroscopic coordinates and velocities follow equations of motion given by the Lagrange-Rayleigh equations

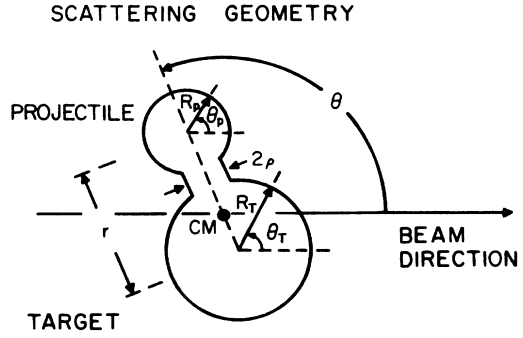

FIG. 16. Scattering geometry for the dynamical reaction model as described in the text.

$$\left[\frac{d}{dt}\frac{\partial}{\partial \dot{\bar{q}}_i} - \frac{\partial}{\partial \bar{q}_i}\right] L = -\frac{\partial}{\partial \dot{\bar{q}}_i} F \,, \tag{4.8}$$

where the index i runs over all reaction variables. In Eq. (4.8) the quantity $L = T - V$ is the Lagrangian and F is the dissipation function. The kinetic energy T is calculated for the two spherical reaction partners, while the neck is taken into account in calculating the interaction potential V and the dissipation function. The motion along the mass, charge, and neck coordinates is assumed to be overdamped by the strong one-body friction forces, such that dynamical driving forces for these coordinates are determined by the balance

$$\partial L / \partial \bar{q}_i = \partial F / \partial \dot{\bar{q}}_i \tag{4.9}$$

of conservative and dissipative forces.

The equations of motion [cf. Eq. (4.8)] are, in the model, coupled to a Fokker-Planck equation describing the fluctuative widths in the N and Z asymmetries. This Fokker-Planck equation can be written as

$$\frac{d}{dt}P(N,Z,t) = \left[-\frac{\partial v_N}{\partial N} - \frac{\partial v_Z}{\partial Z} + \frac{\partial^2 D_{NN}}{\partial N^2} + \frac{\partial^2 D_{ZZ}}{\partial Z^2}\right] \times P(N,Z,t) \tag{4.10}$$

for the time evolution of the joint probability, $P(N,Z,t)$, for finding N neutrons and Z protons on, say, the projectile-like fragment at a given time t. Drift and diffusion coefficients, v, and D, respectively, have been calculated microscopically by Randrup.[17,18] They fulfill the generalized Einstein relations

$$v_i = D_{ii} F_i / \tau_i^* \,, \quad i = N, Z \tag{4.11}$$

where F_i denotes the dynamical force driving the system along the coordinate i and τ_i^* is a measure of the energy interval about the Fermi level contributing to the exchange of nucleons between the reaction partners. The quantities τ_i^* are usually larger than the thermodynamic temperature τ and are strongly dependent on the kinetic energy of relative motion of the fragments. As a consequence, the one-body transport model[17,18] predicts, for a given average displacement of a variable from its original value, fluctuations that are significantly larger than expected from an equilibrium-statistical process.

Equation (4.11) can, in particular, be applied to the total kinetic energy loss, yielding in an approximate[17] fashion

$$D_{EE} \approx \dot{E}_{\text{loss}} \tau^* \tag{4.12}$$

for the relation between the energy diffusion coefficient D_{EE} and the average energy dissipation rate $\dot{E}_{\text{loss}}$.

In the numerical calculations the drift coefficients have been expanded to first order around the average trajectory $\{N(t), Z(t)\}$, as described previously.[5] This procedure yields[5] coupled linear differential equations of motion for the first and second moments of P which are integrated along the average system trajectory. To obtain an estimate for the fluctuations in energy loss associated with each trajectory or impact parameter, Eq.

(4.12) has also been integrated along the trajectory. The model calculations have been discussed in some detail elsewhere.[1,18,76]

Different cuts through the multiparameter potential energy surface assumed in the model calculations for the $^{137}Au + {}^{51}V$ reaction are displayed in Figs. 17 and 18. In Fig. 17 equipotential contour lines for the initial mass and charge asymmetries are plotted versus the relative center separation r and the radius ρ of the neck between the spherical fragments, given in units of the half-density radius[1] C_P of the projectile. At any given touching distance between the fragments, the neck radius is assumed to be at least as large as the radius of the overlap zone. Hence, there is a forbidden region of smaller neck radii, as indicated in Fig. 17. The figures displayed at various contour lines are given in units of MeV. The potential energy surface has been arbitrarily normalized to zero at $r = R_{SA}$ and $\rho = 0$.

The potential shown in Fig. 17 for angular momentum $l = 0$ exhibits a steep gradient resisting decreasing center separations r and increasing neck radii ρ. The first property is simply due to the strong Coulomb repulsion that overcompensates for the nuclear attraction, except for relatively small separations, of the order of 9 fm or less, where a plateau appears to develop in the surface. The resistance of the system against the formation of necks with larger radii is, in the model, due to the disappearance of the proximity attraction between the juxtaposed surface elements, as the corresponding surface area becomes smaller with increasing neck radius.

Several system trajectories are superimposed on the energy surface of Fig. 17, corresponding to initial angular momenta of $l = 130$, 170, and 200, respectively. For the two larger l values, the neck is seen to develop along the geometrical path of minimum radius until the turning point is reached, where the radial kinetic energy vanishes. In the exit channel, the neck radius stays relatively large, due to the strong damping of the neck motion. The motion of the neck follows approximately the steepest gradient of the potential, until it suddenly snaps at a relatively large center separation r.

The $l = 130$ trajectory also depicted in Fig. 17 leads to

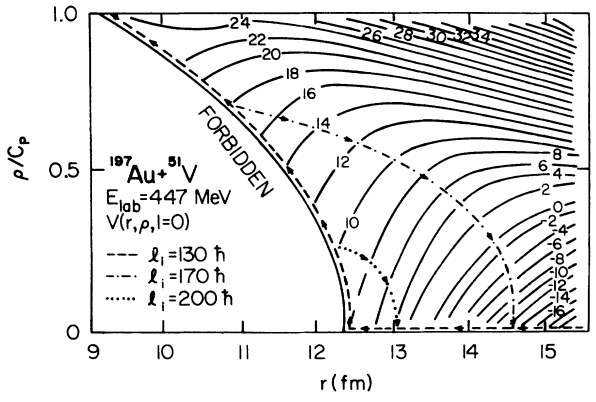

FIG. 17. Potential energy surface for $l = 0$ as a function of reduced neck radius and distance r. Superimposed are trajectories with $l = 130\hbar$ (dashed), $l = 170\hbar$ (dotted-dashed), and $l = 200\hbar$ (dotted) lines.

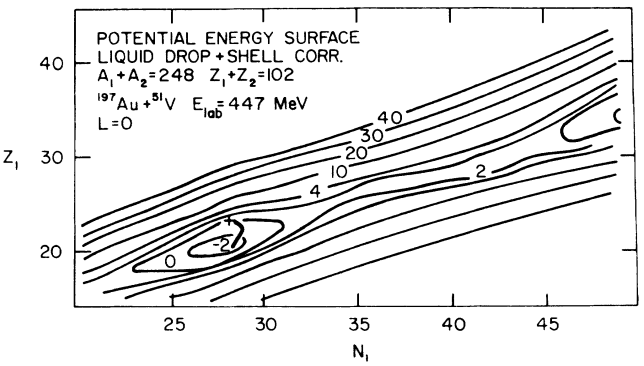

FIG. 18. $l = 0$ potential energy surface is plotted vs proton and neutron number of one of the fragments, as calculated from the liquid-drop model including shell corrections. The cross marks the injection point, and the heavy line represents the trajectory resulting from the dynamical model for a range of l values.

relatively large interpenetrations, forcing the neck to assume a radius approaching that of the projectile. The corresponding shapes represent limiting cases beyond which the shape parametrization employed in the calculations becomes unrealistic. These most compact shapes accommodated by the model describe a mononucleus, rather than a dinucleus. Hence, for $\rho/C_P = 1$, fusion is assumed to have occurred, and the numerical integration is terminated. It appears conceivable, however, that the mononuclear system remembers the initial mass asymmetry at even somewhat later stages of the shape evolution, such that its breakup would not lead to symmetric mass and charge splits characteristic of fusion-fission–like reactions. Therefore, the theoretical angular momenta for which $\rho \rightarrow C_P$ is predicted to occur, calculated in this work, represent only upper limits to the critical angular momentum for fusion. The slight overestimate by the model of the experimental cross section for fusion-fission–like events could be due to such an effect. To evaluate this possibility, however, requires further study.

A different cut through the potential energy surface is exhibited in Fig. 18, where the sum of fragment binding energies and of the nuclear and Coulomb interaction potentials is plotted versus atomic number, Z_1, and neutron number, N_1, of one of the fragments from the reaction $^{197}Au + {}^{51}V$. Considered for this plot were spherical fragments without a neck, on a particular point along the reaction path, the entrance-channel strong-absorption distance. The surface in Fig. 18 is normalized to zero at the initial projectile-target asymmetry identified by a cross mark. Numbers at the individual contour lines give the potential energy in units of MeV.

The potential energy surface in Fig. 18 has the topology of an elongated valley with rather steep walls and a global minimum at symmetric fragmentations. This minimum, which is seen to develop on the right-hand side of the contour diagram, is due to the overall liquid-drop-model[77] energetics. Of more interest for the present purpose is the topology of the surface near the

injection point. Here, a local minimum is observed the potential, caused by the $N=28$ shell closure. This shell minimum is separated from the liquid-drop minimum at symmetry by a broad Businaro-Gallone saddle. The characteristic local structure seen in Fig. 18, however, disappears when the centrifugal energy of orbital motion is added to this potential, resulting in an effective potential energy surface exhibiting only a deep minimum at symmetric fragmentations, or when the separation distance is reduced substantially.

In comparison with the energetics encountered in the $^{197}Au + {}^{51}V$ reaction, the injection point for the $^{165}Ho + {}^{56}Fe$ reaction[7] is located a few MeV higher on the slope of the corresponding energy surface and further removed from a local minimum than that of the $^{197}Au + {}^{51}V$ system. Whereas the nucleon exchange mechanism in the latter reaction starts to develop close to the bottom of the shell-related minimum, which is rather shallow, in the $^{165}Ho + {}^{56}Fe$ reaction, this process explores the topology of the energy surface in the vicinity of the Businaro-Gallone saddle. Although the typical curvatures of the potential energy surfaces are rather small for either reaction, it has been shown[5] that they can, nevertheless, introduce significant correlations in the joint probability distribution for the final fragment masses and charges. They can, in principle, also influence the shape of the fragment Z distribution, an effect not considered in the present implementation of the transport model.

The actual potential governing the exchange of mass and charge between the reaction partners depends on many variables simultaneously and varies dynamically along the system trajectory. It is interesting to note, however, from Fig. 18 that the projection of the system trajectory predicted by the model calculation terminates in the shell-related minimum of the $l=0$ potential energy surface. This trajectory, represented by the heavy curve starting from the injection point on the surface, is drawn through points $(\bar{N}_1,\bar{Z}_1)$ resulting for the final fragment average neutron and proton numbers from the calculations performed for a range of l values from $130<l<230$.

In Sec. IV A an l-wave decomposition of the data was performed assuming a monotonic (sharp) correlation between the initial orbital angular momentum l and an associated average energy loss $E_{\rm loss}$. However, due to the stochastic nature of the energy dissipation mechanism, fluctuations are expected in the $E_{\rm loss}$ variable, for each fixed l value. Integrating Eq. (4.12) along the collision trajectory, one obtains the relation between variance, $\sigma^2_{E_{\rm loss}}$, of the $E_{\rm loss}$ probability distribution and average energy loss $E_{\rm loss}$, depicted in Fig. 19. Here, the average energy loss provides an implicit angular-momentum scale, as illustrated by the bottom parts of Fig. 13. It can be inferred from Fig. 19 that the energy loss associated with a given l value is not too well defined. The widths, FWHM, of the $E_{\rm loss}$ distributions are usually of the same order as the average values. From these model estimates, one would predict a considerable mixing of different l waves in data binned according to $E_{\rm loss}$ or related quantities.

A quantitative comparison is made in Fig. 20 between the experimental angle-energy correlation and the predictions of the dynamical model calculations described above. The experimental points in this $(E,\theta_{\rm c.m.})$ plot

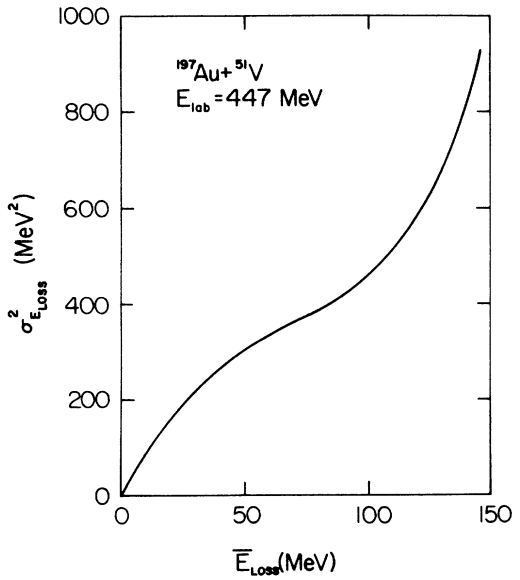

FIG. 19. Relation between average energy loss $E_{\rm loss}$ and variance $\sigma^2_{E_{\rm loss}}$ for the damped reaction $^{197}Au + {}^{51}V$ at $E_{\rm lab}=447$ MeV.

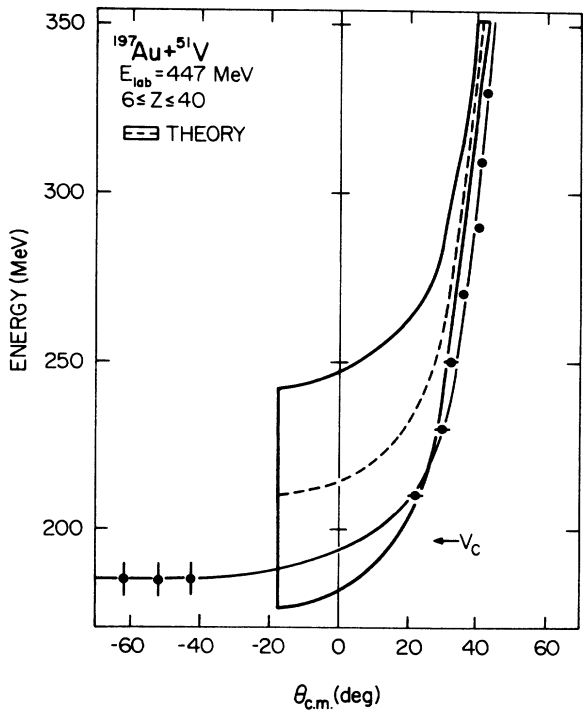

FIG. 20. Experimental and theoretical (dashed line) correlations between total kinetic energy and reaction angle. The solid line represents a smooth interpolation of the experimentally derived maximum cross section. The arrow indicates the Coulomb barrier V_C.

and the solid curve connecting them are derived from the experimental Wilczyński diagram of Fig. 6 based on the orbiting assumption, as discussed in Sec. IV A. The dashed curve in Fig. 20 represents the model calculations for the average correlation between final energy and reaction angle. The solid curves outline a band defined by the FWHM of the energy loss distribution predicted for each l value. As can be inferred from Fig. 20, the general shape of the average experimental correlation is well reproduced by the theory, which predicts negative-angle scattering to occur for a range of initial l values above the critical angular momentum for fusion. However, the theoretical locus of maximum cross section is consistently forward of the experimental one by approximately $\Delta\theta_{\text{c.m.}} \approx 5°$, for most l values. For relatively small angular momenta leading to scattering to small positive or to negative angles, this discrepancy increases. This is interpreted in terms of an underestimation by the model of the extent to which the intermediate system can deform in a strongly damped collision. It possibly also reflects an inadequacy of the family of theoretical dinuclear shapes assumed in the model.

A comparison between the width of the theoretical energy-angle correlation shown in Fig. 20 with the experimental Wilczyński diagram of Fig. 6 demonstrates an underestimation of the experimental widths of the energy distributions, observed as a function of reaction angle $\theta_{\text{c.m.}}$, by more than a factor of 2. However, the qualitative trend seen in the forward-going ridge of Fig. 6 is reproduced by the calculations. It is not surprising to find that the experimental widths of this cross section ridge cannot be reproduced well in the above simplified approach assuming the same deflection angle for all events in the energy loss distribution for a given l value. Taking proper account of the mutual correlations between l, E_{loss}, and $\theta_{\text{c.m.}}$ can be expected to broaden the theoretical band of Fig. 20.

Further predictions of the dynamical transport model are compared to experimental data on the correlations between moments of the fragment Z distribution in Figs. 10 and 11 and to deduced l-dependent quantities in Fig. 13. The confrontation of the empirically derived evolution of interaction times, deflection angle, and total kinetic energy loss with decreasing initial angular momentum with the predictions, exhibited in Fig. 13, illustrates the predictive power of the transport model.

As can be seen from the bottom part of Fig. 13, the empirically deduced dependence of the total kinetic energy loss on angular momentum or impact parameter is well understood in terms of the strong one-body friction force assumed in the model, except for the highest energy losses associated with large system deformations. Furthermore, the experimental deflection function depicted in the middle part of Fig. 13 is well represented by the solid curve resulting from the calculations, with the exception taken in the context of the above discussion of Fig. 20. The good agreement observed for both these correlations implies that the combination of conservative and dissipative forces employed in the dynamical calculations has a realistic radial dependence and overall strength. Furthermore, the predicted interaction times depicted at the top of Fig. 13 are found to be consistent with the values derived in the simple phenomenological analysis of data.

Inspection of Figs. 10 and 11 demonstrates, furthermore, the ability of the transport model to explain the observed dependence of the average charge of the projectile-like fragment and its dispersion on the total kinetic energy loss. This applies also to the correlations with respect to the modified energy loss parameter E^*_{loss} describing the dissipated energy above the Coulomb barrier. In these two figures, the solid curves correspond to calculations neglecting fluctuations in the $E_{\text{loss}}(l)$ distributions, while dashed curves represent theoretical results which have been properly averaged over these E_{loss} distributions, calculated as described above. The agreement between measurement and either model prediction is not perfect, but remarkable for a model calculation in which parameters have not been adjusted to fit the data. Inclusion of the above energy fluctuations results in a somewhat better representation of the dependence of the average charge (Z) of projectile-like fragments on E_{loss} or E^*_{loss} and provides also a good description of the charge variances, except for the highest energy losses. However, for most of the measured energy loss range, the two different sets of calculations fit the data with equivalent accuracy.

The effect of particle evaporation from the primary reaction fragments has been explored for a few values of total kinetic energy loss. Model predictions for the distributions in primary atomic and mass numbers, and for the average intrinsic excitation energies and spins of these fragments, have been used as input parameters for an evaporation calculation employing the computer code PACE.[78] These computations indicated a relatively insignificant change in the model predictions including or excluding sequential fragment decay, as compared with the quoted accuracies of the experimental data.

Comparing the performance of the transport model with respect to fragment charge distributions in the reactions $^{197}\text{Au} + {}^{51}\text{V}$ and $^{165}\text{Ho} + {}^{56}\text{Fe}$, it is apparent that the shapes and centroids of these distributions are better reproduced by the model in the case of the former reaction. The energy-differential fragment Z distributions for the $^{165}\text{Ho} + {}^{56}\text{Fe}$ reaction are more asymmetric and exhibit larger shifts in peak position than observed in the present study, where these distributions are more Gaussian and show less drift with increasing energy loss. Asymmetric, non-Gaussian distributions, however, cannot be described accurately within the scheme of approximations made in solving the Fokker-Planck equation of Eq. (4.10). It seems worthwhile to explore whether asymmetric fragment distributions such as observed[7] for the $^{165}\text{Ho} + {}^{56}\text{Fe}$ and other reactions can be reproduced within the framework of the transport model when the restriction of the theoretical description of the probability distributions $P(N,Z,t)$ in terms of only two moments is relaxed.

As a final topic of interest in the comparison of the present $^{197}\text{Au} + {}^{51}\text{V}$ data with the one-body transport model, the following discussion will briefly return to the question[40,41] as to whether or not a reduced strength

$c_W < 1.0$ of the effective "wall friction" is more appropriate than the nominal strength $c_W = 1.0$ used in friction model calculations such as outlined in this section. From a classical model calculation attempting to reproduce the damping of giant multipole vibrations, Nix and Sierk[41] deduced a strength of $c_W = 0.27$ for the "wall friction." To illustrate the effect of such a reduction on the model predictions, in the case of the damped $^{197}Au + {}^{51}V$ reaction, theoretical c.m. deflection angles $\theta_{c.m.}$ and the first two moments of the fragment Z distributions, $\langle Z \rangle$ and σ_Z^2, respectively, are plotted in Fig. 21 versus E_{loss}. Predictions are made for $c_W = 1.00$ (solid curves) and $c_W = 0.27$ (dashed curves). One can infer from this figure that the maximum possible energy loss suffered in a $^{197}Au + {}^{51}V$ collision is predicted to decrease by about 25 MeV if the reduced value of c_W is adopted instead of $c_W = 1.00$. For low or intermediate energy losses, the difference between the two sets of calculations is negligibly small. This is a consequence of the relatively small contribution of the "wall friction" associated with the type of neck motion considered by the model. The dominant effect of a finite neck size on the frictional energy loss is due to the fully open window inside the neck, facilitating nucleon exchange.

The transport model in its present implementation has been designed mainly for application to rather peripheral heavy-ion collisions, where the effect of the "wall friction" is quite small compared to that of the "window friction." Therefore, a comparison between data and the two sets of calculations for $c_W = 0.27$ and 1.00 shown in Fig. 21 can realistically not be expected to contribute significant information on the strength of c_W. Taking, however, at face value also the model predictions for energy losses approaching complete damping, a reduction $c_W < 1.0$ leads to theoretical E_{loss} dependencies of deflection angle $\theta_{c.m.}$ and of the first two moments, $\langle Z \rangle$ and σ_Z^2, of the fragment charge distribution that provide a poorer representation of the data than the predictions with $c_W = 1.0$. The effect of a reduced "wall friction" on the fragment Z distributions demonstrated in Fig. 21 is partially compensated for by fluctuations in the final total kinetic energies, treated as described earlier. This can be inferred by comparing the solid with the dashed theoretical curves depicted in Figs. 10 and 11.

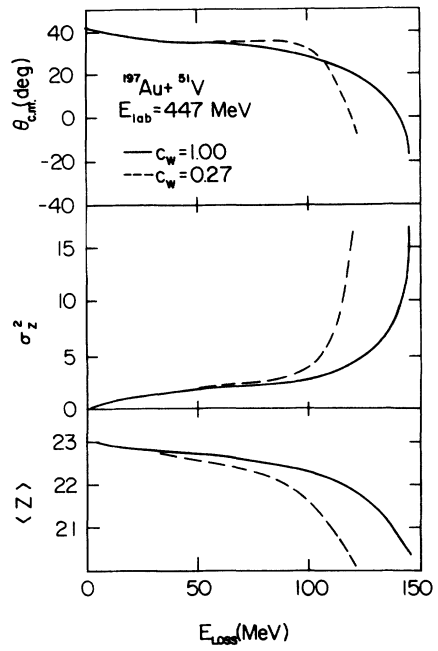

FIG. 21. E_{loss} dependencies of deflection angle, variance, and centroids of Z distribution are plotted for the $^{197}Au + {}^{51}V$ reaction, as predicted for nominal ($c_W = 1.0$, solid curves) and reduced ($c_W = 0.27$, dashed curves) "wall friction."

Although the predictions of the transport model for the very highest energy losses should not be taken too literally, the above discussion illustrates the general ambiguity of interpretations of very strongly damped events. The outcome of such collisions is significantly influenced by both the strength of the dissipative forces and the distribution of energy among the various collective degree of freedom of the system, effects that cannot be disentangled easily.

V. CONCLUSIONS

Collision phenomena ranging from elastic scattering to fusion-fission–like processes have been studied for the $^{197}Au + {}^{51}V$ reaction at $E_{lab} = 447$ MeV. Emphasis has been placed on the investigation of damped reaction features reflected in fragment angular, energy, and charge distributions, as well as in correlations between observables.

Fragment angular distributions are characterized by a sideways peaked, partially damped component, superimposed on a forward-tending distribution indicative of negative-angle scattering in very strongly damped collisions. The time evolution of damped reaction processes is clearly reflected in the dependence of angular and Z distributions on the amount of kinetic energy dissipated in a collision. The measured correlations between experimental observables have been used to deduce the angular-momentum dependence of various reaction parameters and estimates of reaction times. In contrast to observations made with similar systems the energy-differential fragment Z distributions for the $^{197}Au + {}^{51}V$ reaction are relatively well described in terms of Gaussian shapes with centroids that drift slightly to larger asymmetries, as energy is dissipated in a collision. General features of the fragment Z and energy distributions are found to be in approximate overall agreement with systematics established from other studies, although their functional form is not well represented by the predictions of a global fit to many experimental correlations.

Detailed comparisons have been made between experimental correlations and the predictions of dynamical calculations based on a theory of exchange-induced transport. Satisfactory agreement is observed between data and calculations. Experimental average angle-energy correlations are well approximated by the model, for low and intermediate energy losses, although there is a systematic displacement of the theoretical correlation to

more forward angles than experimentally observed. The development of the first and second moments of the Z distributions of projectile-like fragments with increasing energy loss is quantitatively accounted for by the model. A similar observation applies to the comparison of theoretically predicted dependencies of interaction time, deflection angle, and energy loss on initial orbital angular momentum, with those deduced from experimental data. Fluctuations in the correlation between energy loss and impact parameter have approximately been incorporated in the numerical calculations. For low and intermediate energy losses, their effect on the predicted first and second moments of the fragment Z distribution is only of the order of the experimental uncertainties. Improved calculations, considering the correlations between kinematical variables in more detail are needed, in order to provided a better description of the Wilczyński cross section ridges. It has also been demonstrated in the present work that the model predictions are not very sensitive to the absolute magnitude of the "wall friction" force. In view of the fact that no model parameters have been adjusted in the calculations to fit the experimental data, an impressive overall agreement of the experimental fragment distributions and the one-body transport model is observed for the damped $^{147}Au + {}^{51}V$ reaction, lending further support to the dominance of a damped reaction mechanism in which transport phenomena are induced by the stochastic exchange of independent nucleons between the collision partners.

ACKNOWLEDGMENTS

The active participation of Dr. J. R. Birkelund and Dr. W. W. Wilcke and their many helpful comments in the experiment are gratefully acknowledged. His continuous interest and the contribution made by Dr. J. R. Huizenga to this work are highly appreciated. One of us (L.M.S.) wishes to express his gratitude to Dr. H. Bucka for his support and encouragement. The authors also wish to thank Dr. R. J. McDonald for his assistance with the experiments. The efficient operation of the Lawrence Berkeley Laboratory SuperHILAC accelerator, due to the efforts of H. Grunder, R. Stevenson, and the operating crew, was greatly appreciated. This work was supported by the U.S. Department of Energy.

*Present address: Xerox Corporation, Joseph C. Wilson Center for Technology, 800 Phillips Rd., Webster, NY 14580.

[1]W. U. Schröder and J. R. Huizenga, in *Treatise on Heavy-Ion Science,* edited by D. A. Bromley (Plenum, New York, 1984), Vol. 2, Chap. 3, and references cited therein.

[2]W. U. Schröder, J. R. Birkelund, J. R. Huizenga, K. L. Wolf, and V. E. Viola, Jr., Phys. Rep. **45**, 301 (1978).

[3]W. U. Schröder, J. R. Birkelund, J. R. Huizenga, W. W. Wilcke, and J. Randrup, Phys. Rev. Lett. **44**, 308 (1980).

[4]W. W. Wilcke, J. R. Birkelund, A. D. Hoover, J. R. Huizenga, W. U. Schröder, V. E. Viola, Jr., K. L. Wolf, and A. C. Mignerey, Phys. Rev. C **22**, 128 (1980).

[5]W. U. Schröder, J. R. Huizenga, and J. Randrup, Phys. Lett. **98B**, 355 (1981).

[6]H. J. Wollersheim, W. W. Wilcke, J. R. Birkelund, J. R. Huizenga, W. U. Schröder, H. Freiesleben, and D. Hilscher, Phys. Rev. C **24**, 2114 (1981).

[7]A. D. Hoover, J. R. Birkelund, D. Hilscher, W. U. Schröder, W. W. Wilcke, J. R. Huizenga, H. Breuer, A. C. Mignerey, V. E. Viola, Jr., and K. L. Wolf, Phys. Rev. C **25**, 256 (1982).

[8]J. R. Birkelund, H. Freiesleben, J. R. Huizenga, W. U. Schröder, W. W. Wilcke, K. L. Wolf, J. P. Unik, and V. E. Viola, Jr., Phys. Rev. C **26**, 1984 (1982).

[9]A. C. Mignerey, K. L. Wolf, D. G. Raich, V. E. Viola, Jr., J. R. Birkelund, W. U. Schröder, and J. R. Huizenga, Phys. Rev. C **29**, 158 (1984).

[10]H. C. Britt, B. H. Erkkila, A. Gavron, Y. Patin, R. H. Stokes, M. P. Webb, P. R. Christensen, O. Hansen, S. Pontoppidan, F. Videbaek, R. L. Ferguson, F. Pasil, G. R. Young, and J. Randrup, Phys. Rev. C **26**, 1999 (1982).

[11]J. N. De and S. K. Samaddar, Phys. Rev. C **30**, 1763 (1984).

[12]J. N. De, K. Krishan, and S. K. Samaddar, J. Phys. G **10**, L257 (1984).

[13]D. Schüll, W. C. Shen, M. Freiesleben, R. Bock, D. Bang, W. Pfeffer, and F. Pühlhofer, Phys. Lett. **102B**, 116 (1981).

[14]M. Freiesleben and J. V. Kratz, Phys. Rep. **106**, 1 (1984).

[15]R. Vandenbosch, A. Lazzarini, D. Leach, D.-K. Lock, A. Ray, and A. Seamster, Phys. Rev. Lett. **52**, 1964 (1984).

[16]K. Sapotta, R. Bass, V. Hartmann, H. Noll, R. E. Renfordt, and K. Stelzer, Phys. Rev. C **31**, 1297 (1985).

[17]J. Randrup, Nucl. Phys. **A307**, 319 (1978); **A327**, 490 (1979); **A383**, 468 (1982).

[18]T. Døssing and J. Randrup, Nucl. Phys. **A433**, 215 (1985); **A433**, 280 (1985).

[19]D. H. E. Gross and H. Kalinowski, Phys. Rep. **45**, 175 (1978).

[20]W. Nörenberg, Phys. Lett. **52B**, 289 (1974).

[21]W. Nörenberg, Z. Phys. A **274**, 241 (1975).

[22]W. Nörenberg, J. Phys. (Paris) Colloq. **37**, C5-141 (1976).

[23]W. Nörenberg, GSI Report 79-5, 1979.

[24]G. Wolschin, Nukleonika **22**, 1165 (1977).

[25]G. Wolschin and W. Nörenberg, Z. Phys. A **284**, 209 (1978).

[26]M. Dakowski, A. Gobbi, and W. Nörenberg, Nucl. Phys. **A378**, 189 (1982).

[27]A. C. Merchant and W. Nörenberg, Z. Phys. A **308**, 315 (1982).

[28]H. Feldmeier and H. Spangenberger, Nucl. Phys. **A428**, 223c (1984).

[29]H. Feldmeier and H. Spangenberger, Nucl. Phys. **A435**, 229 (1985).

[30]D. H. E. Gross and K. H. Hartmann, Phys. Rev. C **24**, 2526 (1981).

[31]Y. Abe, C. Grégoire, and H. Delagrange, Research Institute for Fundamental Physics (Kyoto) Report RIFP-659, 1986.

[32]U. Brosa and S. Grossman, J. Phys. G **10**, 933 (1984).

[33]R. A. Broglia, C. H. Dasso, and A. Winther, Phys. Lett. **53B**, 301 (1974).

[34]R. A. Broglia, C. H. Dasso, and A Winther, Phys. Lett. **61B**, 113 (1976).

[35]R. A. Broglia, O. Civitarese, C. H. Dasso, and A. Winther, Phys. Lett. **73B**, 405 (1978).
[36]R. A. Broglia, C. H. Dasso, G. Pollarola, and A. Winther, Phys. Rev. Lett. **41**, 25 (1978).
[37]H. Esbensen, A. Winther, R. A. Broglia, and C. H. Dasso, Phys. Rev. Lett. **41**, 296 (1978).
[38]C. H. Dasso, T. S. Dumitrescu, and A. Vitturi, Nucl. Phys. **A378**, 100 (1982).
[39]S. K. Samaddar, J. N. De, and K. Krishan, Phys. Rev. C **31**, 1053 (1985).
[40]J. J. Griffin and M. Dworzecka, Nucl. Phys. **A455**, 611 (1986).
[41]J. R. Nix and A. J. Sierk, in Proceedings of the Workshop on Nuclear Dynamics IV, Copper Mountain, Colorado, CONF-860270 1986, p. 1.
[42]J. Błocki, Y. Boneh, J. R. Nix, J. Randrup, M. Robel, A. J. Sierk, and W. J. Swiatecki, Ann. Phys. (N.Y.) **113**, 330 (1978).
[43]H. J. Wollersheim, W. W. Wilcke, J. R. Birkelund, and J. R. Huizenga, Phys. Rev. C **25**, 338 (1982).
[44]S. Gralla, J. Albinski, R. Bock, A. Gobbi, N. Hermann, K. D. Hildenbrand, J. Kuzminski, W. F. J. Müller, M. Petrovici, M. Stelzer, J. Töke, H. J. Wollersheim, A. Olmi, P. R. Mautenzig, and A. A. Stefanini, Phys. Rev. Lett. **54**, 1898 (1985).
[45]S. Bjørnholm and W. J. Swiatecki, Nucl. Phys. **A391**, 471 (1982).
[46]J. R. Birkelund and J. R. Huizenga, Annu. Rev. Nucl. Sci. **33**, 265 (1983).
[47]H. Breuer, A. C. Mignerey, V. E. Viola, K. L. Wolf, J. R. Birkelund, D. Hilscher, J. R. Huizenga, W. U. Schröder, and W. W. Wilcke, Phys. Rev. C **28**, 1080 (1983).
[48]D.-K. Lock, R. Vandenbosch, and A. Lazzarini, Nucl. Phys. **A384**, 241 (1982).
[49]J. P. Kosky, W. W. Wilcke, J. R. Birkelund, M. A. Butler, A. D. Dougan, J. R. Huizenga, W. U. Schröder, and H. J. Wollersheim, Phys. Lett. **133B**, 153 (1983).
[50]D. Hilscher, J. R. Birkelund, A. D. Hoover, W. U. Schröder, W. W. Wilcke, J. R. Huizenga, A. C. Mignerey, K. L. Wolf, H. F. Breuer, and V. E. Viola, Jr., Phys. Rev. C **20**, 576 (1979).
[51]J. B. Moulton, J. E. Stephenson, R. P. Schmitt, and G. J. Wozniak, Nucl. Instrum. Methods **157**, 325 (1978).
[52]W. E. Frahn and R. H. Venter, Ann. Phys. (N.Y.) **24**, 243 (1963).
[53]W. E. Frahn, Phys. Rev. Lett. **26**, 568 (1971).
[54]W. E. Frahn, Ann. Phys. (N.Y.) **72**, 524 (1972).
[55]W. E. Frahn, Nucl. Phys. **A302**, 301 (1978).
[56]H. Rossner, J. R. Huizenga, and W. U. Schröder, Phys. Rev. C **33**, 560 (1986), and references cited therein.
[57]S. Cohen, F. Plasil, and W. J. Swiatecki, Ann. Phys. (N.Y.) **82**, 557 (1974).
[58]T. Ericson and V. Strutinski, Nucl. Phys. **9**, 689 (1959).
[59]R. Vandenbosch and J. R. Huizenga, *Nuclear Fission* (Academic, New York, 1973).
[60]L. G. Moretto, S. K. Blau, and A. J. Pacheco, Nucl. Phys. **A364** 125 (1981).
[61]J. Q. Li and G. Wolschin, Phys. Rev. C **27**, 590 (1983).
[62]H. H. Rossner, D. Hilscher, E. Holub, G. Ingold, U. Jahnke, H. Orf, J. R. Huizenga, J. R. Birkelund, W. U. Schröder, and W. W. Wilcke, Phys. Rev. C **27**, 2666 (1983).
[63]B. B. Back, H.-G. Clerc, R. R. Betts, B. G. Glagola, and B. D. Wilkins, Phys. Rev. Lett. **46**, 1068 (1981).
[64]M. B. Tsang, H. Utsunomiya, C. K. Gelbke, W. G. Lynch, B. B. Back, S. Saini, P. A. Baisden, and M. A. McMahan, Phys. Lett. **129B**, 18 (1983).
[65]B. B. Back, R. R. Betts, U. Cassidy, B. G. Glagola, J. E. Gindler, L. E. Glendenin, and B. D. Wilkins, Phys. Rev. Lett. **50**, 818 (1983).
[66]K. T. Lesko, D. K. Lock, A. Lazzarini, R. Vandenbosch, V. Metag, and H. Doubre, Phys. Rev. C **25**, 872 (1982).
[67]M. B. Tsang, D. Ardouin, C. K. Gelbke, W. G. Lynch, Z. R. Xu, B. B. Back, R. Betts, S. Saini, P. A. Baisden, and M. A. McMahan, Phys. Rev. C **28**, 747 (1983).
[68]A. Gavron, P. Eskola, A. J. Sierk, J. Boissevain, H. C. Britt, K. Eskola, M. M. Fowler, H. Ohm, and J. B. Wilhelmy, Phys. Rev. Lett. **52**, 589 (1984).
[69]W. J. Swiatecki, Phys. Scr. **24**, 113 (1981).
[70]W. J. Swiatecki, Nucl. Phys. **A376**, 275 (1982).
[71]J. P. Bondorf, M. I. Sobel, and D. Sperber, Phys. Rep. **15**, 83 (1974).
[72]V. E. Viola, Jr., Nucl. Data Sect. **A1**, 391 (1966); Phys. Rev. C **31**, 1550 (1985).
[73]A. Menchaca-Rocha and M. E. Brandan, Phys. Rev. C **24**, 2777 (1981).
[74]M. Brack, J. Damgaard, A. S. Jensen, H. C. Pauli, V. M. Strutinski, and C. Y. Wong, Rev. Mod. Phys. **44**, 320 (1972).
[75]G. Rudolph, A. Gobbi, H. Stelzer, U. Lynen, A. Olmi, H. Sann, R. G. Stokstad, and D. Pelte, Nucl. Phys. **A330**, 243 (1979).
[76]W. U. Schröder, R. T. DeSouza, J. R. Huizenga, and L. M. Schmieder, in *Festschrift and Proceedings of the International Symposium on Nuclear Fission and Heavy-Ion-Induced Reactions,* edited by W. U. Schröder (Academic, Chur, 1987), Vol. 11, p. 255.
[77]W. D. Myers and W. J. Swiatecki, Ark. Fys. **36**, 343 (1967).
[78]M. Hillman and Y. Eyal, Proceedings of the European Conference on Nuclear Physics with Heavy Ions, Caen, 1976, Communications, p. 109; A. Gavron, Phys. Rev. C **20**, 230 (1980).